

2008

Novel wiregrid micropolarizers for infrared imaging polarimetry

Zhi Wu
University of Dayton

Follow this and additional works at: https://ecommons.udayton.edu/graduate_theses

Recommended Citation

Wu, Zhi, "Novel wiregrid micropolarizers for infrared imaging polarimetry" (2008). *Graduate Theses and Dissertations*. 6487.
https://ecommons.udayton.edu/graduate_theses/6487

This Thesis is brought to you for free and open access by the Theses and Dissertations at eCommons. It has been accepted for inclusion in Graduate Theses and Dissertations by an authorized administrator of eCommons. For more information, please contact mschlangen1@udayton.edu, ecommons@udayton.edu.

NOVEL WIREGRID MICROPOLARIZERS FOR INFRARED
IMAGING POLARIMETRY

Thesis

Submitted to

The School of Engineering of the
UNIVERSITY OF DAYTON

in Partial Fulfillment of the Requirements for

The Degree

Master of Science in Electro-Optics Graduate Program

by

Zhi Wu

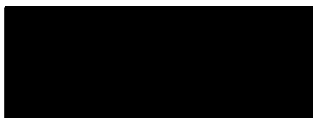
UNIVERSITY OF DAYTON

Dayton, Ohio

August, 2008

NOVEL WIREGRID MICROPOLARIZERS FOR INFRARED IMAGING POLARIMETRY

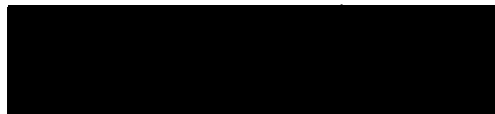
APPROVED BY:



Qiwen Zhan, Ph.D.
Advisor
Associate Professor
Electro-Optics Graduate Program
University of Dayton



Andrew M. Sarangan, Ph.D.
Advisor
Associate Professor
Electro-Optics Graduate Program
University of Dayton



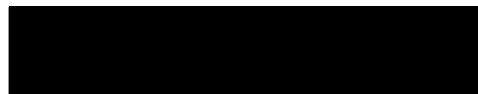
Joseph W. Haus, Ph.D.
Committee Member
Professor and director
Electro-Optics Graduate Program
University of Dayton



Peter E. Powers, Ph.D.
Committee Member
Associate Professor
Electro-Optics Graduate Program
University of Dayton



Malcolm W. Daniels, Ph.D.
Associate Dean
School of Engineering
University of Dayton



Joseph E. Saliba, Ph.D., P.E.
Dean, School of Engineering
University of Dayton

ABSTRACT

NOVEL WIREGRID MICROPOLARIZERS FOR INFRARED IMAGING POLARIMETRY

Wu, Zhi
University of Dayton

Advisors: Dr. Andrew M. Sarangan and Dr. Qiwen Zhan

The majority of infrared imaging systems display the intensity distribution of the light, although some advanced systems also include spectral information. The polarimetric content of an image is an extra degree of information that can be used to enhance and identify objects for applications in remote sensing, surveillance and target tracking. Integrating an array of micropolarizers directly onto the imaging focal plane array is one of the techniques for achieving real-time imaging polarimetry. Although bulk sheet polarizers are commonly available they cannot be patterned into pixel-sized elements. The metal wiregrid polarizer is a viable option and is compatible with microfabrication processes. In this work, a novel design that incorporates a thin layer of silica between the metal grating layer and the silicon substrate is implemented for improving the polarizer performance.

The design and analysis of the micropolarizer is conducted with the rigorous coupled-wave analysis (RCWA). The model is used to predict the extinction ratio and transmission performance of the polarizer in terms of its design parameters. The fabrication processes using deep-UV projection lithography and deep-UV laser interference lithography are introduced, discussed, and compared. The micropolarizer sample with a grating period of 400 nm, grating duty cycle of 0.7, and grating height of 140 nm is fabricated using deep-UV projection lithography. The extinction ratio and transmission coefficient of the micropolarizer is measured with a tunable infrared laser source, which is achieved by optical parametric generator process. Transmission coefficient for p-polarization higher than 70% with extinction ratio higher than 10^4 is achieved for the midwave infrared region. The extinction ratio remains better than 10^2 for the near infrared region above 1.5 μm .

ACKNOWLEDGEMENTS

I would like to thank Dr. Andrew Sarangan and Dr. Qiwen Zhan, my advisors, for their time and effort to direct this thesis and my graduate study. Their patient guidance opened the door of the field of electro-optics, especially in the areas of nano-fabrication, RCWA and surface plasmons. I would also like to thank Dr. Peter Powers for his profound help in sample testing and nonlinear optics theory and Dr. Joseph Haus for the discussion about surface plasmons on metallic grating structure and refractive index sensors.

And many thanks to Dr. Aziz Mahfoud Familia for micropolarizer fabrication and introduction to interference lithography system, to NCSU NNIN facility for ASML system for micropolarizer fabrication, to Weibin Chen for AFM scanning, and to Emily Fehrman, Agus Widjaja, Lirong Sun for their introduction to cleanroom facilities and fabrication techniques.

I am also grateful to DAGSI for their financial support.

Finally, I would like to thank my parents for their support and care, my brother Dr. Wei Wu and his wife Dr. Ning Duan for their help and suggestions.

TABLE OF CONTENTS

ABSTRACT.....	ii
ACKNOWLEDGEMENTS.....	iv
LIST OF FIGURES	vii
CHAPTER	
I. INTRODUCTION.....	1
1.1 Micropolarizer Arrays for Infrared Imaging Polarimetry.....	1
1.2 Rigorous Coupled-wave Analysis – a Tool for Vector Diffraction Modeling	6
II. MICROPOLARIZER DESIGN USING RIGOROUS COUPLED-WAVE ANALYSIS	
.....	14
2.1 The General Structure of Micropolarizers	14
2.2 Effect of the Period and Selection of Metal for the Grating	15
2.3 Effects of the Grating Height and Grating Duty Cycle.....	18
2.4 Effect of a Thin Silica Layer between the Silicon Substrate and Metal Grating	21
III. FABRICATION TECHNIQUES.....	24
3.1 Deep UV Projection Lithography	24
3.2 Deep UV Laser Interference Lithography	29

3.2.1 Spin Coating Photoresist.....	29
3.2.2 DUVLIL with the Assistance of Mask Aligner	32
3.2.3 Electron-beam Evaporation Deposition.....	40
3.2.4 Lift-off Process	42
3.3 A Comparison of DUVPL and DUVLIL.....	44
IV. MICROPOLARIZER CHARACTERIZATION.....	46
4.1 Introduction to a Tunable Infrared Laser Source	46
4.2 Experimental layout and description	50
4.3 Measurement and Results	53
V. CONCLUSIONS AND FUTURE WORK	56
BIBLIOGRAPHY.....	59

LIST OF FIGURES

Figure 1-1. Images of a static scene for Stokes vector components S_0 , S_1 , and S_2 , respectively. [4].....	4
Figure 1-2. A super pixel in a micropolarizer array.....	5
Figure 1-3. High-spatial-frequency grating structure [9].....	8
Figure 1-4. Three-dimensional binary subwavelength grating diffraction problem. [13]	10
Figure 2-1. Cross sectional view of a micropolarizer	15
Figure 2-2. Performance comparison of different metal grating materials. (a) Extinction Ratio versus incident wavelength curve; (b) TM transmission versus incident wavelength curve.....	17
Figure 2-3. Performance comparison of different grating heights and grating duty cycles. (a) Extinction Ratio versus incident wavelength curve; (b) TM transmission versus incident wavelength curve.	20
Figure 2-4. Performance comparison of different silica thicknesses. (a) Extinction Ratio versus incident wavelength curve; (b) TM transmission versus incident wavelength curve.	23
Figure 3-1. Diagram of the principle of projection lithography [18].....	25

Figure 3-2. Fabrication process using deep UV projection lithography [19].	26
Figure 3-3. SEM image of micropolarizer array with an AFM image shown in the inset.	27
Figure 3-4. Laurell WS400-LITE Photoresist Spinner	30
Figure 3-5. Spin speed curve of UVN 30 [20]	31
Figure 3-6. Absorbance curve of UVN30 [20]	32
Figure 3-7. Layout of DUVLIL system	33
Figure 3-8 MBD-266 deep UV laser	34
Figure 3-9. The diagram of the proposed system comprising the UV beam illuminating on the sample and UV mirror that are mounted on a rotating fixture.	36
Figure 3-10. SEM side view image of grating test pattern of photoresist produce from the interference lithography system under development.	36
Figure 3-11. Suss MA6/BA6 Mask Aligner	37
Figure 3-12. Pixels with pixel numbers	39
Figure 3-13. Principle of electron-beam evaporation deposition [18]	41
Figure 3-14. Diagrams of aluminum grating fabrication for pixels with the same orientation. (a) Diagram of cross sectional view of the silicon wafer after fabricating thin silicon dioxide layer, which is about 50 nm, on the silicon substrate using thermal oxidation; (b) Diagram of cross sectional view of the sample after spin coating UVN 30, which is negative photoresist for DUV; (c) After DUVLIL, using the mask shown as the inset to over expose the pixels for grating orientation other than the desired orientation; (d)	

Diagram of cross sectional view of the sample with top view diagram as an inset after development; (e) Diagram of cross sectional view of the sample with top view diagram as an inset after deposition of ~200 nm aluminum film using electron-beam evaporation. (f) Diagram of cross sectional view of the sample with top view as an inset after lift-off.... 43

Figure 4-1. Experimental setup for optical characterization of micropolarizer. L1 to L3: lenses; M1 to M5: mirrors; BS: beam splitter; HWP: half-wave plate; P1: reflection polarizer; P2: transmission polarizer; F1 and F2: dichromatic filter; PPLN: periodically poled lithium niobate; D1 and D2: detectors; F3: filter for expanding the dynamic range of detector; F4: bandpass filter; MC: monochromator; CC1 and CC2: computer control using LabView; OSC: oscilloscope. 51

Figure 4-2. Experiment results of micropolarizer sample characterization along with simulation results. (a) Extinction ratio versus incident wavelength curve; (b) TM transmission coefficient versus incident wavelength curve. 55

CHAPTER I

INTRODUCTION

1.1 Micropolarizer Arrays for Infrared Imaging Polarimetry

Electromagnetic (EM) waves are vectorial transverse waves with a broad spectral range that includes radio frequency, microwaves, Tera Hertz (THz), infrared (IR), visible (VIS), ultraviolet (UV), X-rays, and gamma-rays. The amplitude (intensity), phase, spectrum, and polarization information carried by these EM waves emitted or reflected from certain objects contains important information, such as the constituting material, temperature, surface quality and orientation, etc. Imaging systems are often used to record the spatial distribution of such information within a field of view. Most of the imaging systems that we are familiar with are optical imaging systems operating in the visible light band, which map the two dimensional distribution of the light emitted or scattered from targets within the field of view. Some of these optical imaging systems only record the intensity information of light, such as black and white photography. Some also record both the intensity distribution and the spectral distribution, such as color

photography. Visible light usually is emitted by objects with very high surface temperatures, which are rarely encountered in our normal environment. For example, a surface temperature of about 6000 K enables the sun, the most important light source to the earth, to emit a broad spectrum that includes the entire visible band. Thus visible light imageries are typically limited to recording scenes under solar radiation or other similar source to illuminate the passive targets. In contrast, IR radiation from thermal or black body radiation, is emitted by most objects at much lower temperatures commonly encountered in our environment. Consequently, IR imaging can be used for imaging objects in the absence of solar or external illumination and for detecting the properties of objects that depend on temperature variations.

Typical IR imagery records intensity distribution, although some systems also include spectral information as additional observables. Recently there has been a growing need to expand the electro-magnetic observables of IR imaging systems to include polarimetric information, which describes how the transverse electrical field vector of the light temporally evolves at a certain spatial point [1]. The polarimetric content of an image provides an extra degree of information that can be used to enhance and identify objects within the scene, which have important applications in remote sensing, surveillance and target tracking [2, 3].

Polarization state of the light can be described by the Stokes vector with its four components defined as [1]:

$$\begin{aligned}
S_0 &= I_0 + I_{90} \\
S_1 &= I_0 - I_{90} \\
S_2 &= I_{45} - I_{135} \\
S_3 &= I_R - I_L
\end{aligned}
\tag{1.1}$$

where I_0 , I_{90} , I_{45} , I_{135} are the intensities of the light polarized in different angles with respect to a fixed axis. I_R is the intensity of right hand circular (RHC) polarization component and I_L is the intensity of left hand circular (LHC) polarization component. In general, intensity measurements with a polarizer oriented at the above 4 different directions will render the first three Stokes parameters. In order to measure the last Stokes parameter, typically a quarter waveplate is required. Several approaches are currently in use. One approach is to take consecutive frames from a single sensor by inserting different polarizers and variable phase retarders. However, this is a slow process and does not lend itself to real-time applications. Another approach is to split the incident beam and use different polarizers and waveplates in the optical path, which can be used in real-time applications. This requires multiple image sensors. One drawback of using multiple image sensors is the precise alignment that is required between the sensors and the requirement to maintain that alignment under all operating conditions. As a result, currently available multi-sensor platforms tend to be large and heavy. Many of these problems can be overcome by directly integrating pixel-sized polarizers on to the imaging sensor.

Real-time images of the first three Stokes parameters have been previously obtained by integrating a wiregrid micropolarizer array directly onto a focal plane array (FPA) [4]. The requirement of a waveplate to measure the last Stokes parameter will be a significant design complexity for imaging systems based on micropolarizer arrays. Consequently, most of the real-time polarimetric imageries only detect the first three Stokes parameters. The second and third Stokes vector components have the capability to highlight or suppress different materials or objects at different orientations (Figure 1-1) [4]. Certain saturated regions in S_0 image can be better observed through S_1 and S_2 images. The difference between S_1 and S_2 images of the roof in Figure 1-1 clearly shows the polarization dependence on surface orientations. Moreover, it is well known that manmade objects have distinct polarization states that can be used to distinguish them from background radiation.

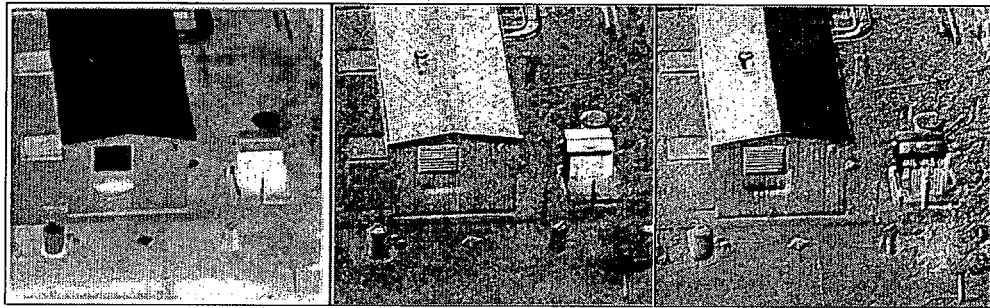


Figure 1-1. Images of a static scene for Stokes vector components S_0 , S_1 , and S_2 , respectively. [4]

Wiregrid polarizers are high spatial frequency metal gratings with periods smaller than the wavelength of incident light in the medium [5-7]. Due to the subwavelength period, diffraction orders other than the zeroth order become evanescent and do not propagate into the far field. A subwavelength grating using metallic material strongly reflects TE polarization (s-polarization) and allows most of the TM polarization (p-polarization) to transmit through, functioning as a linear polarizer rather than as a diffraction grating. For real-time polarimetric imaging, it is necessary to integrate the detector array with a micropolarizer array that has different transmission axes within a group of pixels much like how color filtering is done in visible imaging sensors [4]. Four pixels arranged into 2 x 2 checker board pattern with grating orientations 0 °, 45 °, 90 °, and 135 ° with respect to a specified pixel edge are designed in a group as a super pixel (Figure 1-2).

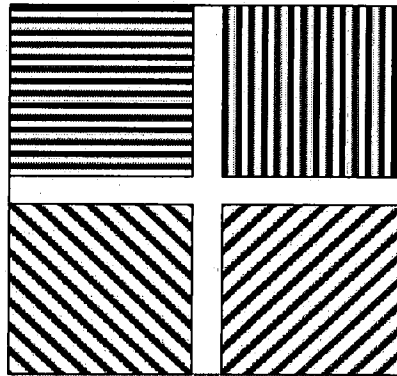


Figure 1-2. A super pixel in a micropolarizer array

The quality of the polarimetric image will be determined by the TM transmission and extinction ratio, which in turn are determined by the period, duty cycle, and height of the metal grating as well as the dielectric structures surrounding the metal grating. In general, the performance of a wiregrid micropolarizer degrades at shorter wavelengths as the wiregrid dimensions approach the wavelength of light in the medium. In previous publications, extinction ratios of around 500 at 5 μm with TM transmission around 70% [4] and an extinction ratio just over 100 in the 2.5 μm – 6 μm range [6] were reported. In this present work, we have significantly improved the extinction ratio and TM transmission of wiregrid micropolarizers using novel design techniques. Our micropolarizers were fabricated using ASML deep-UV projection lithography system by Dr. Aziz Mahfoud. My contribution was mainly on the micropolarizer design, characterization, and deep-UV laser interference lithography.

1.2 Rigorous Coupled-wave Analysis – a Tool for Vector Diffraction Modeling

Optical gratings are periodic structures that play important roles in optical devices and component design and analysis. It is critical to analyze or predict the optical responses of these devices given the device parameters and illumination conditions. In principle, solving Maxwell's equations under certain boundary conditions can give us all the information about the field distribution and propagation inside and outside of these

devices. In practice, it is more desirable to simplify the problem with valid approximations to obtain analytical or numerical solutions. Depending on the grating period relative to the wavelength of incident light in the medium, grating theory in general can be divided into three regimes: scalar diffraction, vector diffraction and effective medium regime.

When the length scale of optical devices is larger than about 10λ , scalar diffraction theory can be safely applied, where λ is the wavelength of incident light in the medium. All components of electric field and magnetic field can be described by the same scalar wave equation [8]

$$\nabla^2 u(r, t) - \frac{n^2}{c^2} \frac{\partial^2 u(r, t)}{\partial t^2} = 0 \quad (1.2)$$

where n is the refractive index of the medium.

If the feature size of optical devices is smaller than about 0.1λ , the structure is indistinguishable on the scale of observation and the medium can be homogenized by the effective medium theory (EMT) using the properties and fractions of the constituting materials. This approach has been widely used for high-spatial-frequency gratings with various applications such as antireflection coating and volume holography [9-12]. For periodic structures, the homogenization problem is typically parameterized with the period-wavelength ratio as a small parameter. Then the effective index can be expressed as a power series of that ratio as [12]:

$$n_{\text{eff}} = n_0 + n_1 (\Lambda/\lambda) + n_2 (\Lambda/\lambda)^2 + \dots \quad (1.3)$$

For a grating structure shown in Figure 1-3, it is equivalent to a uniaxial film with refractive indices n_o and n_e according to the zeroth-order approximation of EMT, where n_o and n_e are given by [9]:

$$n_o^2 = n_1^2 (1 - D) + n_2^2 D \quad (1.4)$$

$$n_e^2 = \frac{n_1^2 n_2^2}{(1 - D)n_2^2 + Dn_1^2} \quad (1.5)$$

D is the duty cycle of region 2 shown in Figure 1-3 and Λ is the grating period.

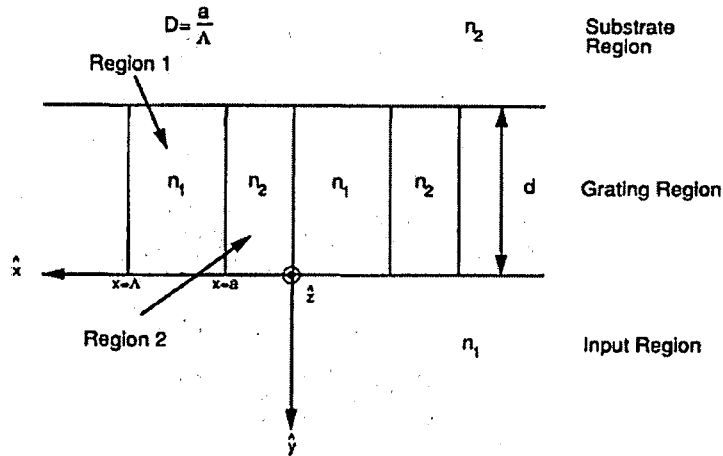


Figure 1-3. High-spatial-frequency grating structure [9]

The zeroth-order usually works very well for structures with extremely small period. If the structures have period close to 0.1λ or better accuracy is desired, higher

order EMT approximations have also been derived. For example, the second-order solutions are [11]

$$\left[n_o^{(2)}\right]^2 = \left[n_o^{(1)}\right]^2 + \frac{1}{3} \left[\pi \frac{\Lambda}{\lambda_0} F(1-F) \right]^2 (n_2^2 - n_1^2)^2 \quad (1.6)$$

$$\left[n_e^{(2)}\right]^2 = \left[n_e^{(1)}\right]^2 + \frac{1}{3} \left[\pi \frac{\Lambda}{\lambda_0} F(1-F) \right]^2 \left(\frac{1}{n_2^2} - \frac{1}{n_1^2} \right)^2 \left[n_e^{(1)}\right]^6 \left[n_o^{(1)}\right]^2 \quad (1.7)$$

For grating structures with period between the scalar diffraction regime and the EMT regime, diffraction phenomena can neither be solved by scalar diffraction theory because of field coupling at subwavelength boundary, nor be solved by EMT, since the structure scale is not small enough to be homogenized. A rigorous diffraction theory that incorporates the vector nature of light as well as the boundary conditions is required. Various types of rigorous diffraction theory have been developed in the past. It can be done either in frequency domain, such as rigorous coupled-wave analysis (RCWA) method [13,14] and Fourier modal analysis method [15], and in space domain, such as finite difference time domain (FDTD) method [16]. For periodic structures, RCWA is a very mature technique and its validity has been proven by many publications. In this study, we also adopted the RCWA method to study metal wiregrids.

The general three-dimensional conical mounting binary subwavelength grating diffraction problem used in RCWA method is depicted in Figure 1-4 [13]. Although a binary grating structure is used as an example, its applicability is not limited to binary gratings [14].

The incident beam is linear polarized with incident angle of θ , and azimuthal angle of ψ . The grating period is Λ ; the duty cycle of region II is f ; and the grating height is d . In the grating region, the periodic relative permittivity is expandable in a Fourier series of the form

$$\varepsilon(x) = \sum_h \varepsilon_h \exp\left(j \frac{2\pi h}{\Lambda} x\right) \quad (1.8)$$

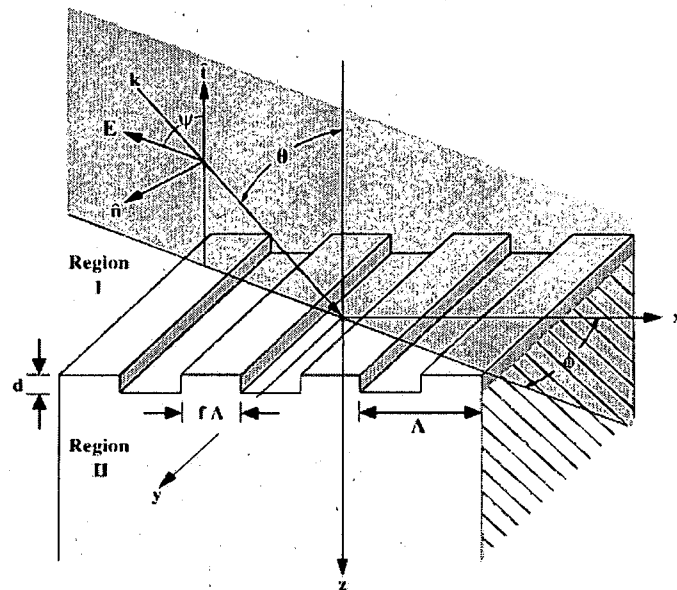


Figure 1-4. Three-dimensional binary subwavelength grating diffraction problem. [13]

For TE polarization, the incident normalized electric field that is normal to the incident plane is given by

$$E_{inc,y} = \exp[-jk_0 n_1 (x \sin \theta + z \cos \theta)] \quad (1.9)$$

where $k_0 = 2\pi/\lambda_0$ and λ_0 is the wavelength of light in free space. The normalized solution in region I and region II are given by

$$E_{I,y} = E_{inc,y} + \sum_i R_i \exp[-j(k_{xi}x - k_{I,zi}z)] \quad (1.10)$$

$$E_{II,y} = \sum_i T_i \exp\{-j[k_{xi}x - k_{II,zi}(z-d)]\} \quad (1.11)$$

where

$$k_{xi} = k_0 [n_l \sin \theta - i(\lambda_0/\Lambda)] \quad (1.12)$$

$$k_{I,zi} = \begin{cases} k_0 [n_l^2 - (k_{xi}/k_0)^2]^{1/2} & k_{xi} > k_0 n_l \\ -jk_0 [(k_{xi}/k_0)^2 - n_l^2]^{1/2} & k_0 n_l < k_{xi} \end{cases} \quad l = I, II \quad (1.13)$$

and i indicates the order number.

With Maxwell's equation

$$H = \left(\frac{j}{\omega\mu} \right) \nabla \times E \quad (1.14)$$

we can finally obtain the solutions of the problem in matrix representation as the following [14]. At input boundary, we can obtain the backward-diffracted amplitudes R_i from Equation (1.10).

$$\begin{bmatrix} \delta_{i0} \\ jn_l \cos \theta \delta_{i0} \end{bmatrix} + \begin{bmatrix} \mathbf{I} \\ -j\mathbf{Y}_l \end{bmatrix} [\mathbf{R}] = \begin{bmatrix} \mathbf{W} & \mathbf{WX} \\ \mathbf{V} & -\mathbf{VX} \end{bmatrix} \begin{bmatrix} \mathbf{c}^+ \\ \mathbf{c}^- \end{bmatrix} \quad (1.15)$$

At output boundary, the forward-diffracted amplitudes T_i can be obtained from Equation (1.11).

$$\begin{bmatrix} \mathbf{WX} & \mathbf{W} \\ \mathbf{VX} & -\mathbf{V} \end{bmatrix} \begin{bmatrix} \mathbf{c}^+ \\ \mathbf{c}^- \end{bmatrix} = \begin{bmatrix} \mathbf{I} \\ j\mathbf{Y}_{II} \end{bmatrix} [\mathbf{T}] \quad (1.16)$$

where $\delta_{i0} = 1$ for $i = 0$, $\delta_{i0} = 0$ for $i \neq 0$, \mathbf{I} is the identity matrix, $\mathbf{V} = \mathbf{WQ}$, \mathbf{W} is the eigenvector matrix of matrix \mathbf{A} , $\mathbf{A} = \mathbf{K}_x^2 - \mathbf{E}$, \mathbf{E} is the matrix formed by the permittivity harmonic components with $e_{ip} = \varepsilon_{(i-p)}$, \mathbf{K}_x , \mathbf{Q} , \mathbf{X} , \mathbf{Y}_I , and \mathbf{Y}_{II} are diagonal matrices with diagonal elements equal to k_{xi}/k_0 , q_m , $\exp(-k_0 q_m d)$, $k_{1,zi}/k_0$, and $k_{II,zi}/k_0$, respectively, q_m are the positive square root of the eigenvalues of the matrix \mathbf{A} , \mathbf{R} is the vector with elements R_i , \mathbf{T} is the vector with elements T_i , and \mathbf{c}^+ and \mathbf{c}^- are unknown constant vectors to be determined by boundary conditions. [14]

Similarly, for TM polarization, the incident normalized magnetic field that is normal to the incident plane is given by

$$H_{inc,y} = \exp[-jk_0 n_1 (x \sin \theta + z \cos \theta)] \quad (1.17)$$

The normalized solution in region I and region II are given by

$$H_{I,y} = H_{inc,y} + \sum_i R_i \exp[-j(k_{xi}x - k_{1,zi}z)] \quad (1.18)$$

$$H_{II,y} = \sum_i T_i \exp\{-j[k_{xi}x + k_{II,zi}(z - d)]\} \quad (1.19)$$

With Maxwell's equation

$$\mathbf{E} = \left(\frac{-j}{\omega \varepsilon_0 n^2} \right) \nabla \times \mathbf{H} \quad (1.20)$$

the backward- and forward-diffracted amplitudes can be represented in matrix format as follows [14].

$$\begin{bmatrix} \delta_{i0} \\ j \cos \theta \delta_{i0} / n_1 \end{bmatrix} + \begin{bmatrix} \mathbf{I} \\ -\mathbf{Z}_1 \end{bmatrix} [\mathbf{R}] = \begin{bmatrix} \mathbf{W} & \mathbf{WX} \\ \mathbf{V} & -\mathbf{VX} \end{bmatrix} \begin{bmatrix} \mathbf{c}^+ \\ \mathbf{c}^- \end{bmatrix} \quad (1.21)$$

$$\begin{bmatrix} \mathbf{WX} & \mathbf{W} \\ \mathbf{VX} & -\mathbf{V} \end{bmatrix} \begin{bmatrix} \mathbf{c}^+ \\ \mathbf{c}^- \end{bmatrix} = \begin{bmatrix} \mathbf{I} \\ j\mathbf{Z}_\Pi \end{bmatrix} [\mathbf{T}] \quad (1.22)$$

where $\mathbf{V} = \mathbf{E}^{-1} \mathbf{WQ}$, \mathbf{W} is the eigenvector matrix of matrix \mathbf{EB} , $\mathbf{B} = \mathbf{K}_x \mathbf{E}^{-1} \mathbf{K}_x - \mathbf{I}$, \mathbf{Q} , \mathbf{Z}_1 , and \mathbf{Z}_Π are diagonal matrices with diagonal elements equal to q_m , $k_{1,zi}/k_0 n_1^2$, and $k_{\Pi,zi}/k_0 n_\Pi^2$, respectively, q_m are the positive square root of the eigenvalues of the matrix \mathbf{EB} , and the other parameters are defined the same as those in the case of TE polarization.

With the matrix representation of the solutions, the problem can be solved efficiently by performing matrix operation numerically. MATLAB codes that can handle TE, TM as well as conical illumination have been developed to implement the RCWA method and used in this study. It is worthy of mentioning that, although the derivation for binary grating was illustrated above for example, our RCWA code can handle arbitrary non-binary periodic structures [14].

CHAPTER II

MICROPOLARIZER DESIGN USING RIGOROUS COUPLED-WAVE ANALYSIS

2.1 The General Structure of Micropolarizers

A micropolarizer array is comprised of wiregrid micropolarizers with different transmission axis orientations. The cross sectional view of a micropolarizer structure is shown in Figure 2-1. It consists of a metal grating on a thin silica layer above a silicon substrate. TM transmission and extinction ratio are determined by the period, duty cycle, and height of the metal grating as well as the dielectric structures surrounding the metal grating. The figure of merit of wiregrid polarizers, usually described by their TM transmission and extinction ratio (TM transmission divided by TE transmission), is optimized by adjusting the structural parameters of the wiregrid design. Since the metal grating has a period on the same order of magnitude as the incident wavelength in the medium, the micropolarizer is designed using the rigorous coupled-wave analysis (RCWA) method [14]. In the model, a plane wave illuminates the metal grating from the

silicon substrate side at normal incidence. The dispersion of metal and silicon is included in the model through cubic spline interpolation of the data from Ref. [17]. The refractive index of silica is chosen to be 1.46 and treated as lossless and dispersionless. In the following 3 sections, the effects of grating material, period, duty cycle and height will be discussed in detail.

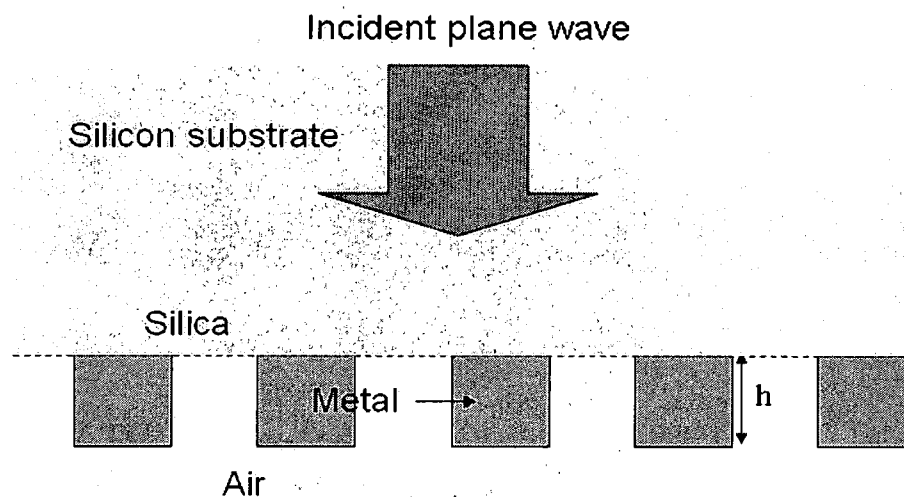


Figure 2-1. Cross sectional view of a micropolarizer

2.2 Effect of the Period and Selection of Metal for the Grating

One of the most important differences between wiregrid polarizers and diffraction gratings is that the periods of wiregrid polarizers are much smaller than those used in

diffraction gratings. Typically, the period of a diffraction grating is on the same order of magnitude as the incident wavelength in the media, while the period of a wiregrid polarizer is subwavelength, i.e., 0.1λ to 0.5λ . For grating period larger than 0.5λ , the TM transmission will begin to decrease significantly due to losses from the diffracted beam. In general, a shorter grating period allows the working range of a wiregrid polarizer to be extended into shorter wavelengths. But the fabrication becomes increasingly more difficult for short grating periods. For our micropolarizer design, the grating period was chosen to be 400 nm, primarily dictated by the practical resolution limit of the projection lithography system that was used for this fabrication.

The material of the grating is another important factor that affects the performance of the micropolarizer. We investigated several metals suitable for making wiregrid polarizers, including Al, Au, and Mo. The simulation results with the same structural parameters are shown in Figure 2-2. Grating height of 200 nm, grating duty cycle of 0.7 and 50 nm silica layer between the grating and the silicon substrate were used.

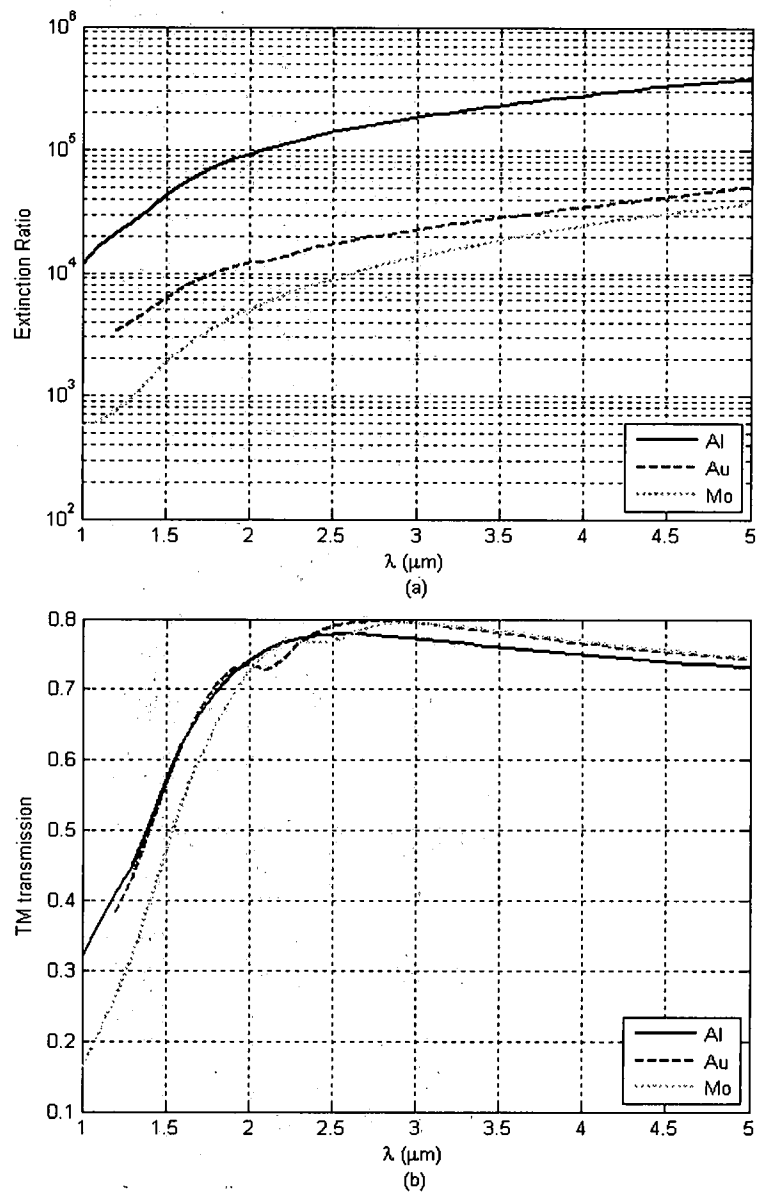


Figure 2-2. Performance comparison of different metal grating materials. (a) Extinction Ratio versus incident wavelength curve; (b) TM transmission versus incident wavelength curve.

In TM transmission versus incident wavelength curve, for wavelengths above 2 μm , the TM transmissions for different metals are close to each other around 0.74 to 0.8. For wavelengths below 2 μm , the TM transmission for Mo drops faster than Al and Au. The reason is, as the wavelength becomes comparable with the grating period, the TM transmission becomes more sensitive to the differences in the material properties of the grating. In this region, the imaginary parts of refractive indices of Au and Al are much larger than that of Mo.

In extinction ratio versus incident wavelength curve, the extinction ratio of Al grating is about 1 order of magnitude higher than that of Au grating and Mo grating. Thus we chose Al as the material to fabricate wiregrid micropolarizer arrays. In addition, Al is inexpensive and the deposition and patterning is relatively easier than other materials.

2.3 Effects of the Grating Height and Grating Duty Cycle

The polarizer performance is significantly affected by the grating height and grating duty cycle. Typically, a larger grating height and a larger duty cycle give a higher extinction ratio, but they also reduce the TM transmission. With a thin silica layer between the metal grating and the silicon substrate, we studied how the grating height and duty cycle would affect the optical characteristics of the micropolarizer. The

thickness of the thin silica layer was chosen to be 50 nm, the function and effect of which will be discussed in next section.

From the extinction ratio versus incident wavelength curve in Figure 2-3, it is clear that the larger the grating height and duty cycle, the higher the extinction ratio. But the performance trade-off between extinction ratio and TM transmission places a limit on duty cycle. When the duty cycle is 0.7, the TM transmission is around 0.75 for grating heights between 200 nm and 400 nm at wavelengths $2.5\ \mu\text{m} - 5\ \mu\text{m}$. The TM transmissions are relatively insensitive to grating height in this wavelength region. When the duty cycle increases to 0.8, TM transmissions decrease below 0.7. The larger the grating height, the lower the TM transmissions become. A smaller duty cycle of 0.6 gives higher TM transmissions, especially at shorter wavelengths. But the change in TM transmissions with grating height varies for different wavelength ranges. For longer wavelengths between $3\ \mu\text{m}$ and $5\ \mu\text{m}$, the TM transmission increases with increasing grating height. On the other hand, for shorter wavelengths between $1.5\ \mu\text{m}$ and $3\ \mu\text{m}$, the TM transmission decreases with increasing grating height. So if we only consider longer wavelengths $3\ \mu\text{m} - 5\ \mu\text{m}$, the larger grating height will give simultaneously higher extinction ratio and TM transmission.

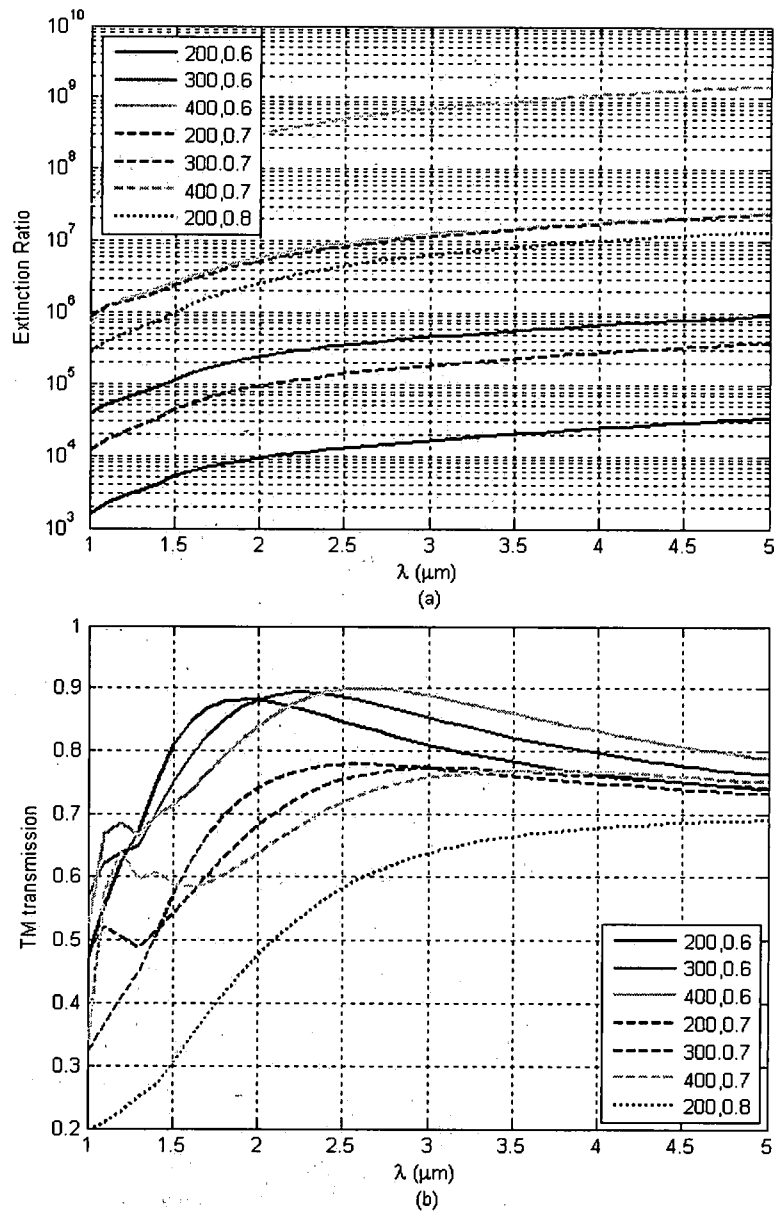


Figure 2-3. Performance comparison of different grating heights and grating duty cycles.
 (a) Extinction Ratio versus incident wavelength curve; (b) TM transmission versus incident wavelength curve.

However, grating height is primarily limited the fabrication process. For example, the depth of focus in the projection lithography limits the thickness of photoresist to about 400 nm at the resolution required to produce the smallest features of the grating. The photoresist grating then serves as the mask for the subsequent deposition and lift-off to produce metal wiregrids. To ensure uniformity across the whole wafer, only a fraction of the photoresist height, typically 30%-50% can be utilized for the lift-off process. This further places a limit on the metal grating height. Details of projection lithography will be discussed in Chapter III-1.

For a grating height fixed at 200 nm, the TM transmissions are close to each other between 3 μm to 5 μm for duty cycles of 0.6 and 0.7. For a duty cycle of 0.8, TM transmission drops rapidly. In order to simultaneously achieve a reasonable performance for both the extinction ratio and TM transmission, the duty cycle was chosen to be 0.7.

2.4 Effect of a Thin Silica Layer between the Silicon Substrate and Metal Grating

The aluminum grating was grown on a thin silica layer produced by thermal oxidation of the silicon substrate. This silica layer plays an important role in the micropolarizer performance. As the refractive index of silica is much lower than that of silicon, the aluminum grating will have a much shorter effective period compared to when the incident wavelength is propagating directly through the silicon substrate.

Consequently the working range of the micropolarizer can be extended to shorter wavelengths with the insertion of the silica layer. This silica layer also isolates the grating from the silicon substrate and reduces the reflected power that propagates into the silicon substrate, thereby improving the TM transmission of the polarizer [6]. The predicted performance with different silica layer thicknesses is shown in Figure 2-4. For layer thicknesses from 20 nm to 200 nm, the extinction ratio increases gradually for wavelengths between 2 μm and 5 μm . On the other hand, for silica layer thicknesses above 100 nm, the TM transmissions become slightly higher at longer wavelengths but decrease sharply at some shorter wavelengths due to the interference of the reflections at the silicon/silica and silica/grating interfaces. In our design, the thickness of the silica layer was chosen to be 50 nm to simultaneously achieve high extinction ratio and TM transmission over a broad working wavelength range. The predicted performance without the silica layer is also shown in Figure 2-4 for comparison, which clearly demonstrates the performance enhancements due to the thin silica layer.

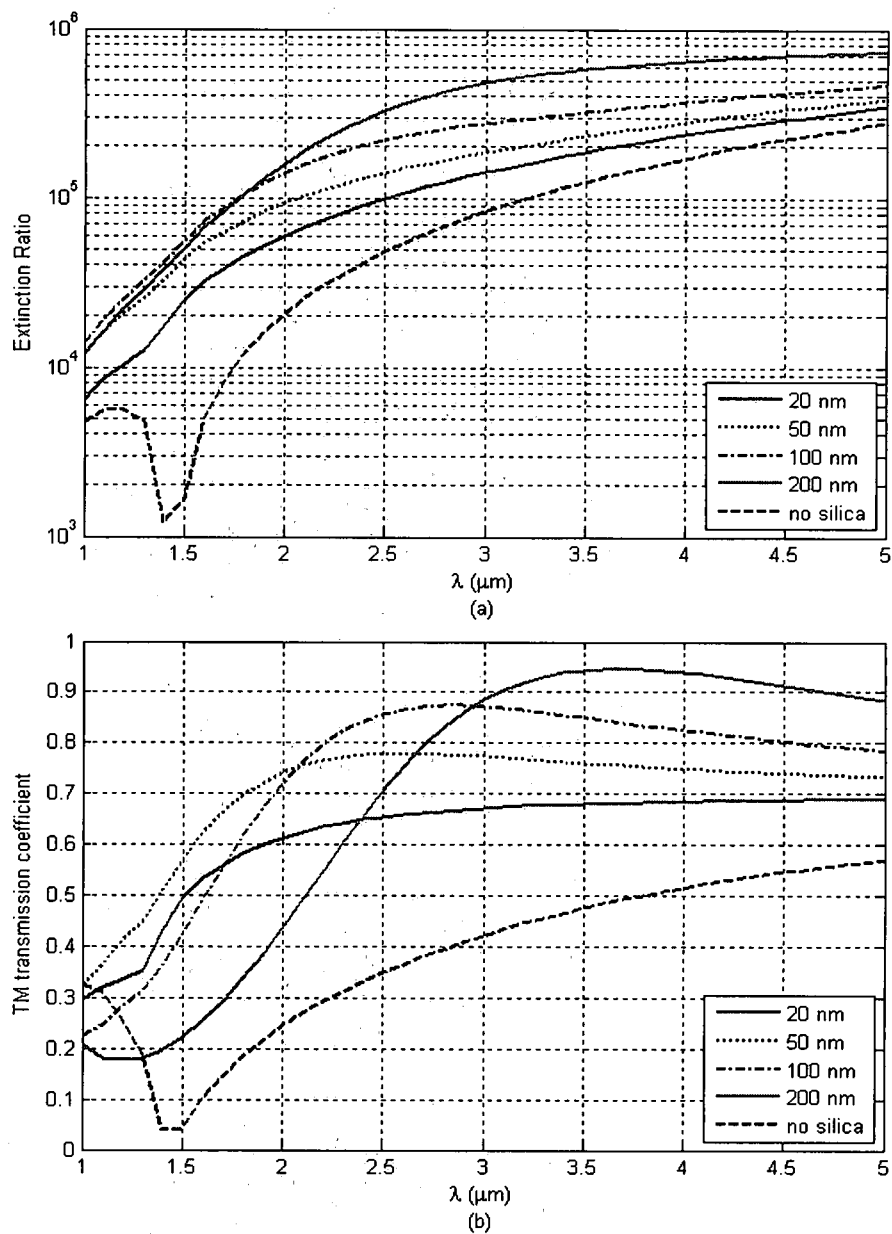


Figure 2-4. Performance comparison of different silica thicknesses. (a) Extinction Ratio versus incident wavelength curve; (b) TM transmission versus incident wavelength curve.

CHAPTER III

FABRICATION TECHNIQUES

3.1 Deep UV Projection Lithography

The micropolarizers were fabricated by deep-UV projection lithography (DUVPL) technique using ASML 5500, which is a state-of-the-art, 193-nm optical scanner available at NCSU.¹

The principle of projection lithography is shown in Figure 3-1 [18]. The light through an aperture is focused on the mask by a condenser lens. An image of the mask is projected on the wafer surface through a projection lens, which reduces the mask image by 4 times. The projected field size is 26 x 32 mm. The image is exposed on the wafer multiple times by stepping the wafer by a fixed distance after each exposure. Stage movement is controlled by laser interferometry with alignment accuracy better than 40 nm. However, this feature was not necessary for our design because the entire

¹ All the wafer processing steps using the ASML 5500 were performed at NCSU-NNIN facility by Dr. Aziz Mahfoud.

micropolarizer array was designed to fall within one field size. Each stepping of the field produced a distinct micropolarizer array. The ultimate image resolution for this system is specified as 130 nm. To achieve such a small resolution, the beam has to be focused tight, which gives a large numerical aperture (NA)

$$NA = \sin \theta_o \quad (3.1)$$

With a large NA, the depth of focus σ becomes small with a relation shown in Equation (3.2) [18].

$$\sigma = \frac{\lambda}{NA^2} \quad (3.2)$$

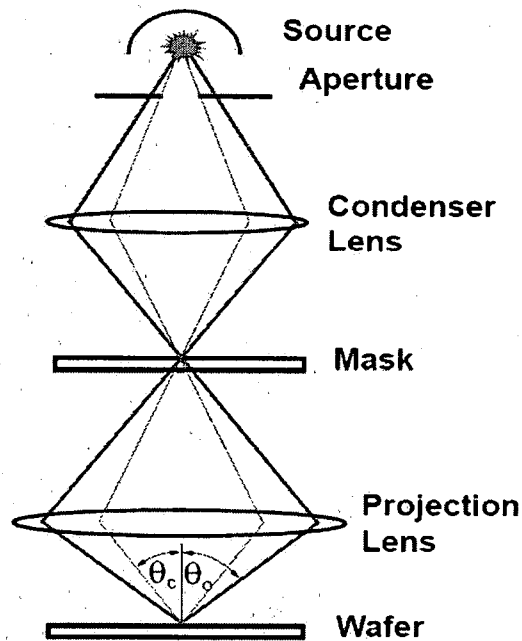


Figure 3-1. Diagram of the principle of projection lithography [18]

In the ASML 5500 system, the NA was about 0.7 in order to achieve a resolution higher than 150 nm. The depth of focus is then only about 400 nm, which limits the maximum of the grating height that can be reliably exposed, and it also places strict requirements on wafer flatness and tilt compensations in the system.

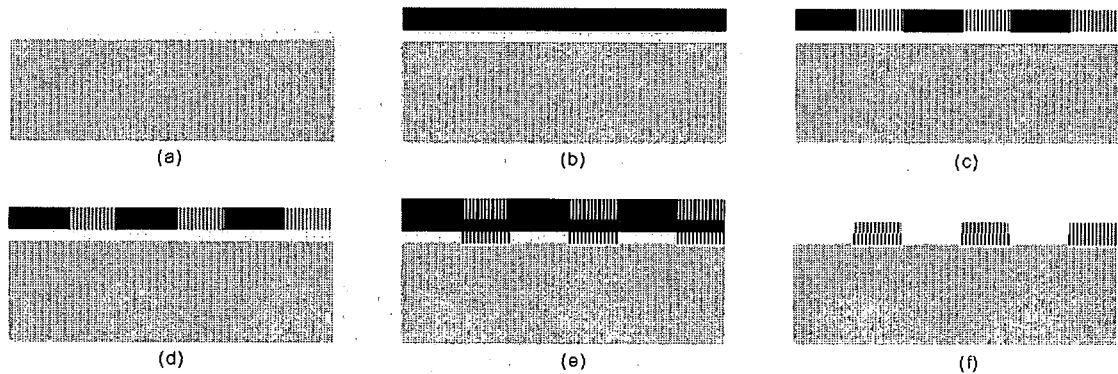


Figure 3-2. Fabrication process using deep UV projection lithography [19].

The fabrication process is outlined in Figure 3-2 [19]. First, a thin layer of silica is grown using thermal oxidation with a thickness of about 50 nm, as discussed in Chapter II-4 for improving the performance of micropolarizer. In the second step, a backside anti-reflected coating (BARC) is spin coated. This is commonly done to avoid the reflection and standing waves from the substrate during the exposure (Figure 3-2 (a)). This is more important in a laser-illuminated exposure than in a lamp-illuminated exposure. Then, a photoresist layer is spin coated for imaging the pattern on the mask (Figure 3-2 (b)). After

this, DUVPL is performed to transfer the pattern on the mask to the photoresist with a 4X image-reduction (Figure 3-2 (c)). Then the BARC and the photoresist layers are etched in an Oxygen plasma so that the Al deposition in the next step would adhere to the substrate instead of the BARC layer (Figure 3-2 (d)). After this step, Al is deposited using evaporation (Figure 3-2 (e)). Finally, the Al deposited on the photoresist was lifted off by dissolution in acetone under ultrasonic agitation. The details about spin coating, electron-beam evaporation deposition, and lift-off process will be discussed in next section.

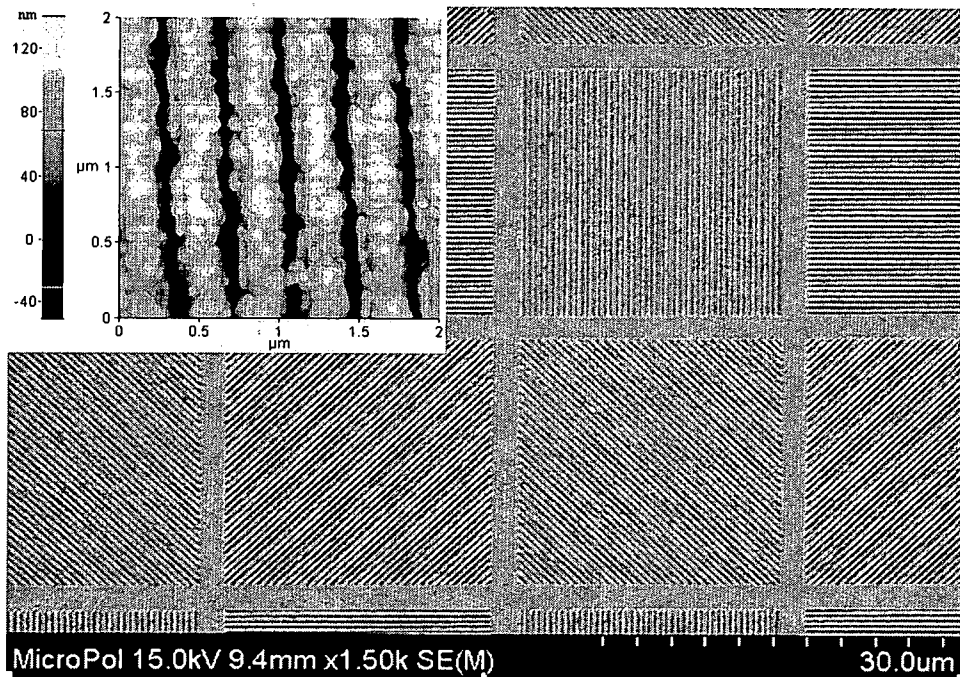


Figure 3-3. SEM image of micropolarizer array with an AFM image shown in the inset.

A scanning electron microscopy (SEM) image of the micropolarizer array fabricated using the above processes is shown in Figure 3-3 with a $2\text{ }\mu\text{m} \times 2\text{ }\mu\text{m}$ atomic force microscopy (AFM) scan shown in the inset. The average metal grating height was determined to be 140 nm from the AFM scan. The whole array is approximately 1 inch \times 1 inch in size and contains 1 million pixels of micropolarizers. The array is arranged into a grid of four pixels (super-pixel) at 0° , 90° , 45° and 135° orientations to enable the computation of the first three Stokes parameters. Each micropolarizer is $25\text{ }\mu\text{m} \times 25\text{ }\mu\text{m}$ with $2.5\text{ }\mu\text{m}$ spacings between pixels. Since each pixel is too small for optical characterization prior to integration with the detector array, a $2.5\text{ cm} \times 1\text{ cm}$ test bar, which was a single wiregrid polarizer with the same fabrication parameters as those applied in the micropolarizer array, was placed adjacent to the micropolarizer array. This allows for a probe laser beam to be used to evaluate the performance of the micropolarizers. Since the micropolarizer pixels are clearly formed with no degradation of the edges, the test bar should be an accurate representation of its performance except for any diffraction effects which should be negligible for this pixel size, especially when directly bonded to the detector surface.

3.2 Deep UV Laser Interference Lithography

The micropolarizer devices that were completed and tested for this project were performed in the AMSL 5500 system. Deep UV laser interference lithography (DUVLIL) is an alternative to projection lithography and is currently under development at the UD Nanofab Laboratory¹. The results shown here are still preliminary. The grating structures are generated by the interference of two coherent laser beams, which are expanded original laser beam and its reflected beam. The period of the interference pattern can be simply adjusted by changing the incident angle to the sample. To realize four adjacent pixels with different orientations, a mask aligner has to be used in conjunction with DUVLIL. The proposed process of doing DUVLIL will be described below. Similar to the DUVPL, a thin layer of silicon dioxide will be grown first using thermal oxidation.

3.2.1 Spin Coating Photoresist

Chemically amplified negative DUV photoresist, UVN30 was used for the processed development of DUVLIL. In order to obtain adequate adhesion, MicroChem Primer 80/20 (MCC Primer 80/20) was spin coated on the thermal oxide layer before

¹ The laboratory was created in 2004 by Dr. Andrew Sarangan with two research grants from the Ohio 3rd Frontier Project.

UVN30. Laurell WS400-LITE Photoresist Spinner (Figure 3-4) was used for spin coating both MCC Primer 80/20 and UVN30.

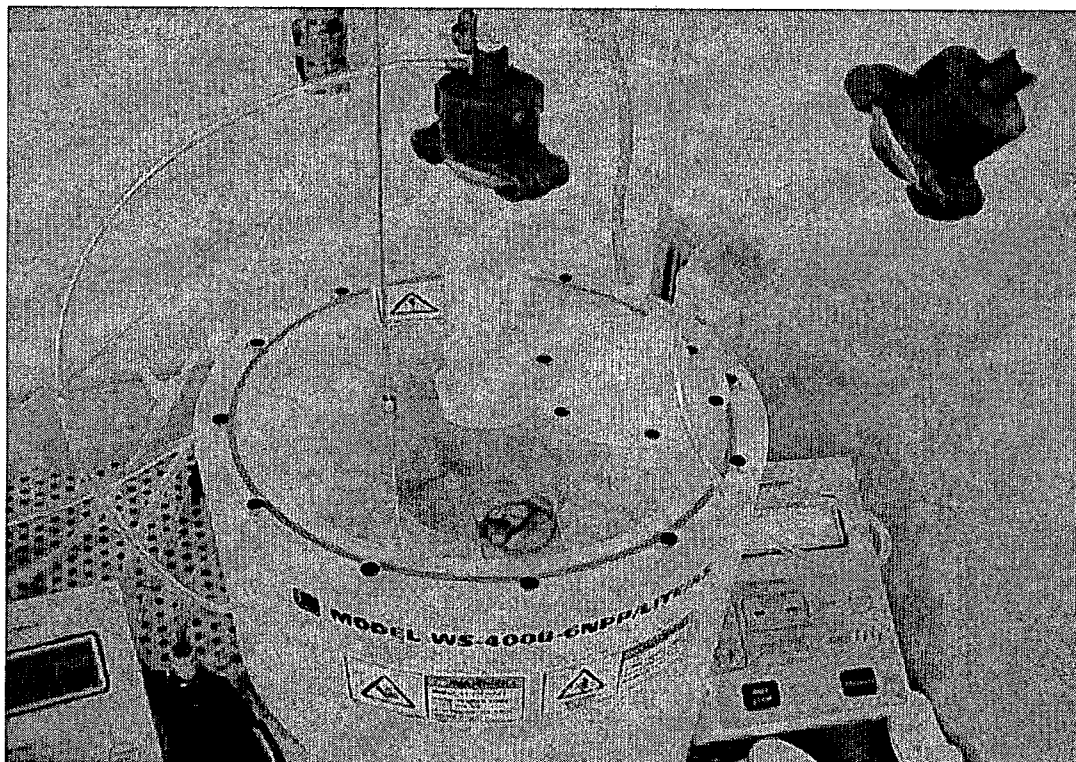


Figure 3-4. Laurell WS400-LITE Photoresist Spinner

The thickness of spin coated resist is related to its solvent content and spin speed. The higher the solvent content, the thinner the resulting resist film. For a fixed solvent content, the thickness of resist reduces with increasing spin speed. The spin speed curve of UVN30 is shown in Figure 3-5 [20]. The sensitivities of the photoresist to different

wavelengths are dependent on the absorbance curve (Figure 3-6 [20]), which is an important parameter for choosing photoresist for different wavelengths. After spin coating, the wafer will be softbaked to evaporate the solvent. Before performing DUVLIL, the sample should be protected from stray UV light.

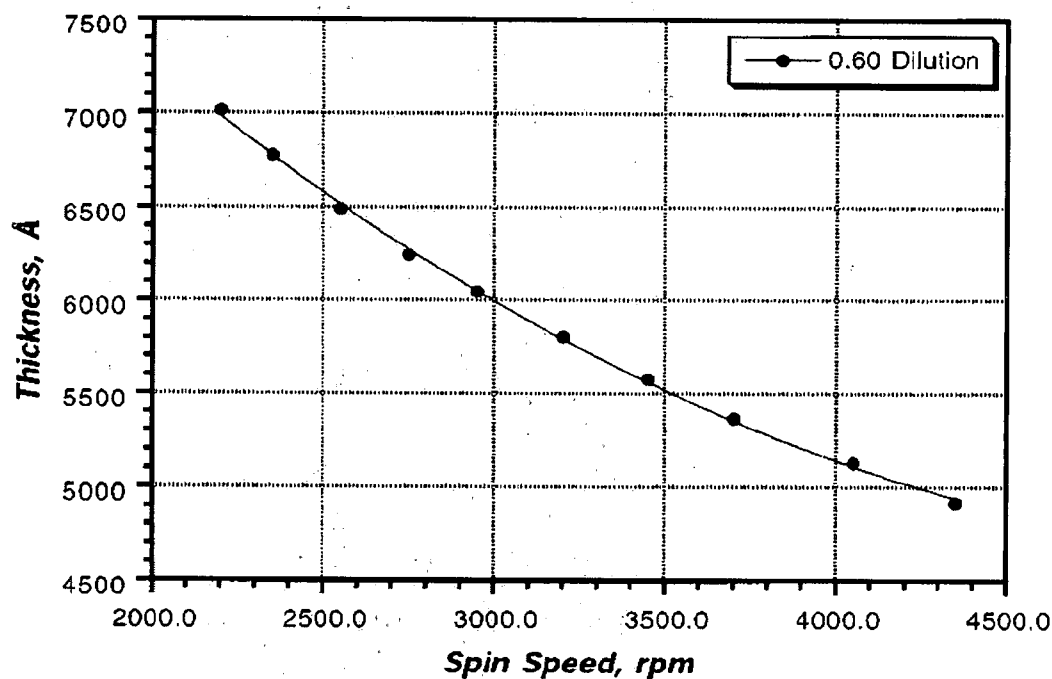


Figure 3-5. Spin speed curve of UVN 30 [20]

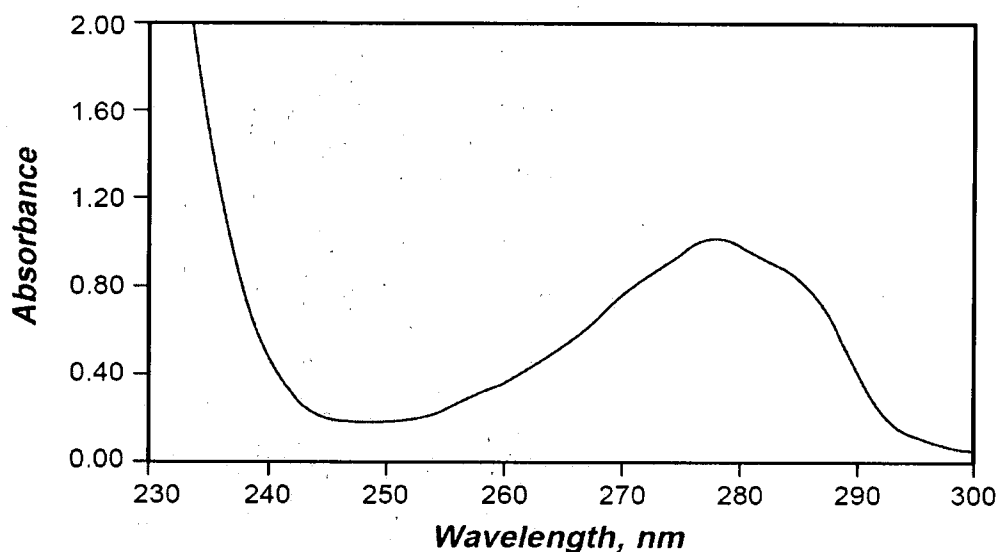


Figure 3-6. Absorbance curve of UVN30 [20]

3.2.2 DUVLIL with the Assistance of Mask Aligner

In order to achieve the micropolarizer array described in Chapter I, DUVLIL has to be used in conjunction with a mask aligner, which can perform precise alignment of a mask and a wafer during photolithography process. As a super pixel is comprised of four micropolarizers with different transmission axes and only one grating orientation can be achieved during a single exposure using DUVLIL, four repeat steps have to be performed using DUVLIL and the mask aligner (Suss MA6 Aligner). A proposed method to realize a micropolarizer array is to use DUVLIL to generate grating patterns with one orientation

each time, and then using the mask aligner to align different masks in order to over expose the undesired pixel areas, which will be dissolved in an acetone lift-off process.

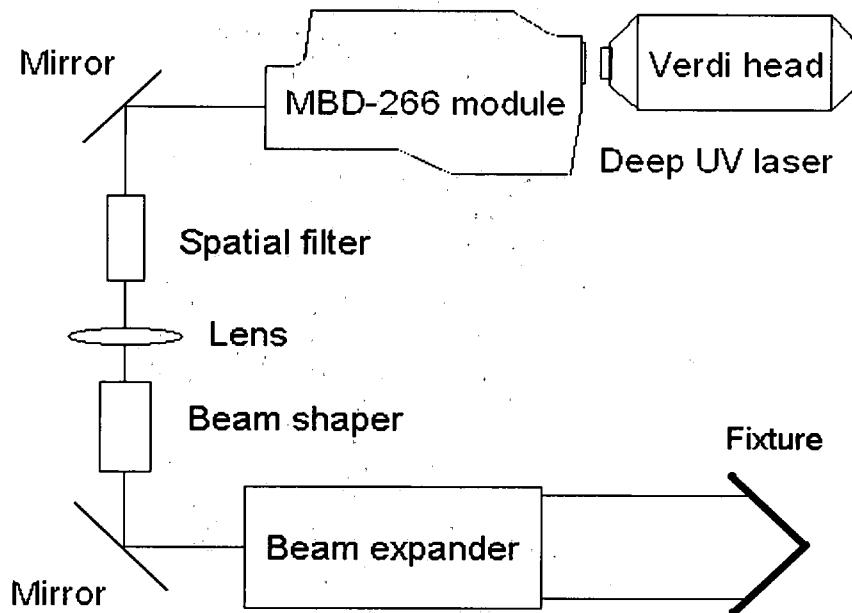


Figure 3-7. Layout of DUVLIL system

The DUVLIL system is built on a Smart Table featuring Newport iQ Damping Technology, which utilizes electro-mechanical vibration dampers to introduce damping into all natural vibration modes in a given range without creating any additional resonances at lower frequencies [21]. The layout of DUVLIL system is shown in Figure 3-7. The Deep UV laser source is MBD-266 (Figure 3-8), which is a solid-state diode-pumped high power deep-UV laser. The laser has two parts, the Verdi head and the

resonant frequency doubling unit. The output of Verdi head is a 532-nm laser beam with a maximum power of 2 W, which is pumped by a diode laser. The green laser beam serves as the input of the resonant frequency doubling unit, which doubles the frequency of the 532-nm laser beam and generates the 266-nm deep-UV laser beam, the maximum power of which is more than 200 mW.

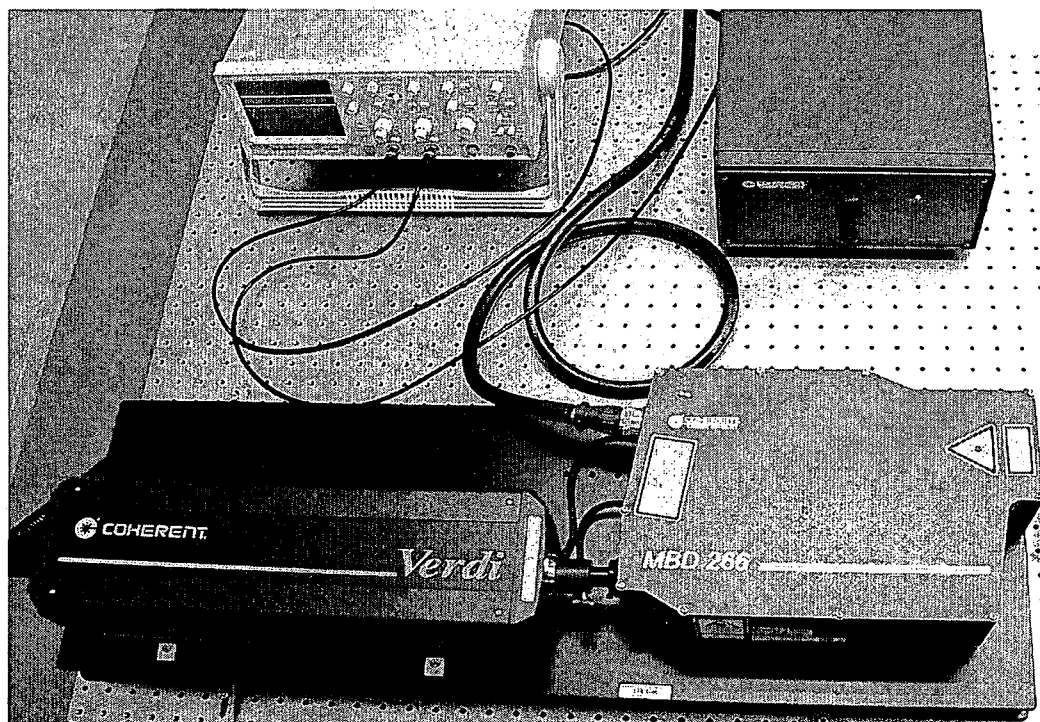


Figure 3-8 MBD-266 deep UV laser

A spatial filter will be used to clean up the beam to TEM_{00} mode. A lens after the spatial filter collimates the beam to a beam size that fits the input beam size of the beam

shaper, which reshapes the beam from a Gaussian-profile beam to a top-hat beam, the diameter of which is about 8 mm. And then the beam is expanded by a beam expander, which is comprised of two lenses. The beam diameter will be up to 4" after the beam expander. The beam then illuminates on a fixture mounted with the sample and a large UV mirror (Figure 3-9). The UV mirror and a metal plate are clipped on the fixture and the sample is sucked onto the metal plate through vacuum holes. The fixture is mounted on a rotation stage. A portion of the beam directly illuminates on the sample, while another portion illuminates on the mirror first and then is reflected on the sample. The two portions of the beam are coherent and generate interference pattern on the sample, which results in different exposure doses to the photoresist that spin coated on the silicon substrate. For negative photoresist, the positions corresponding to dark fringes are washed away after develop; and the positions corresponding to bright fringes remain. Therefore, a grating pattern of photoresist is formed on the silicon substrate. Figure 3-10 shows the scanning electron microscopy (SEM) side view image of the grating pattern of photoresist with a period of about 500 nm most recently fabricated using DUVLIL. The grating profile is quite close to rectangular as expected. By rotating the rotation stage, the incident angle of the UV beam to the sample can be changed, which in turn changes the period of the interference pattern on the sample and hence the period of photoresist grating. Consequently, the period of the micropolarizer can be easily changed.

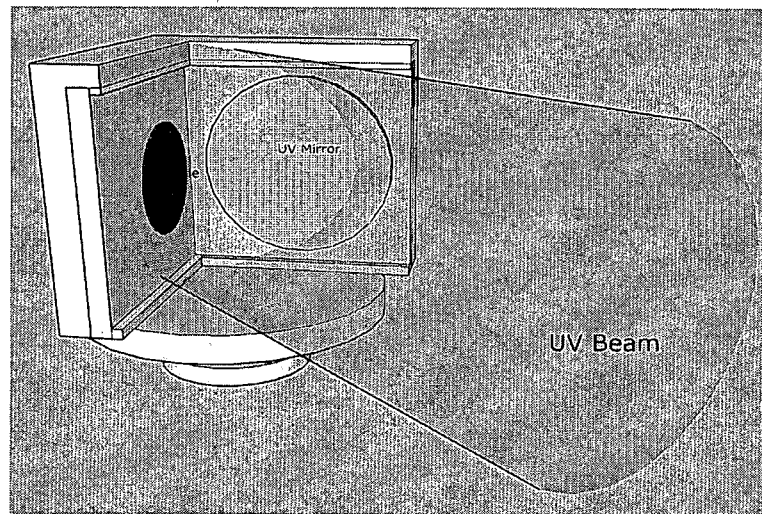


Figure 3-9. The diagram of the proposed system comprising the UV beam illuminating on the sample and UV mirror that are mounted on a rotating fixture.

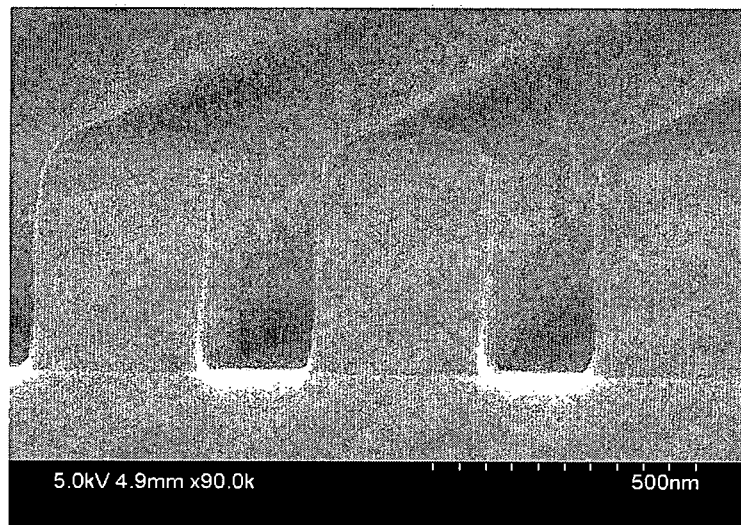


Figure 3-10. SEM side view image of grating test pattern of photoresist produce from the interference lithography system under development

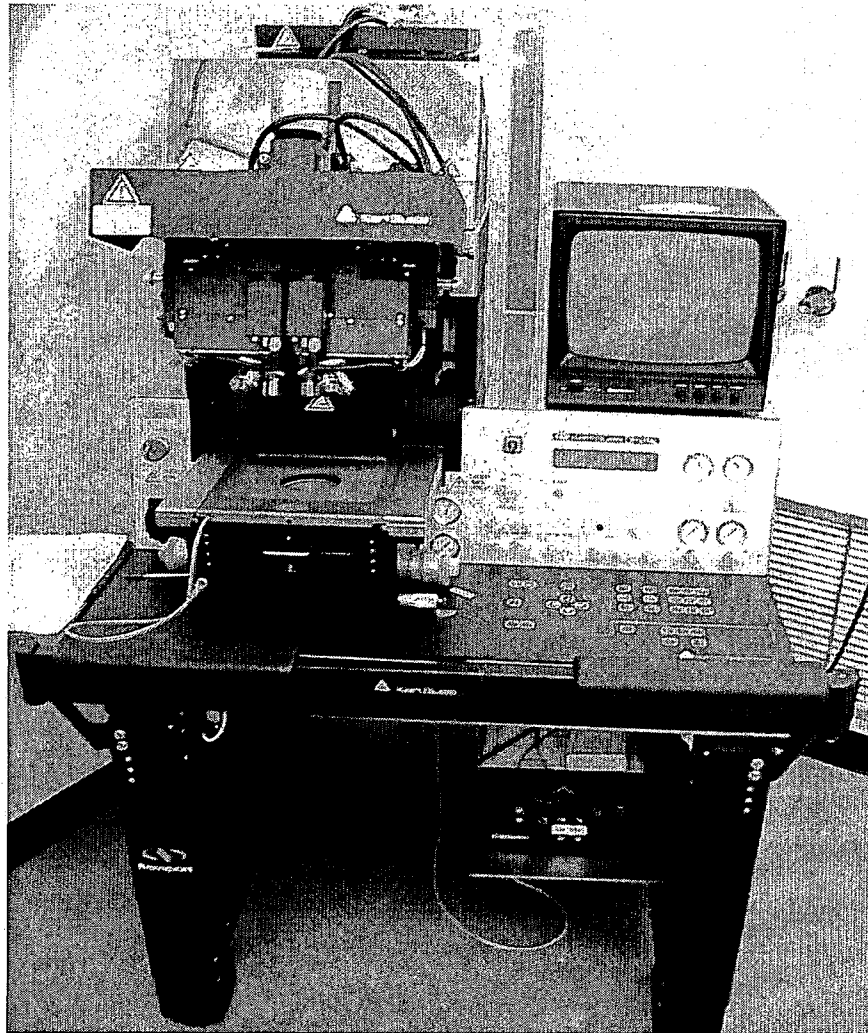


Figure 3-11. Suss MA6/BA6 Mask Aligner

However, to make a micropolarizer array instead of a single large-area polarizer, the mask aligner (Figure 3-11) has to be used for overexposing the undesired pixels

immediately after the exposure in the interference beams. With a microscope, the mask aligner has the ability to align the wafer to the mask precisely, and then do exposure with i-line (365 nm) of mercury lamp. However, the sensitivity of the UVN30 to the i-line is very low, so a very high dosage may be required. Preliminary tests indicate that the sensitivity to i-line may be too low to be practical. An alternative way is only use the mask aligner to align the wafer and the mask and transport it to the DUVLIL setup. After the alignment, the wafer and mask could conceivably stick together by pressing them through vacuum. And then the wafer with the mask can be exposed under the deep-UV source of MBD-266 using the same setup of DUVLIL except normal incidence will be used with a diffuser, because an over exposure will be made this time and there should not be any fringe pattern formed on the sample. This proposed method to fabricate micropolarizer arrays using DUVLIL is still under development.

Sacrificial masks on quartz or fused silica substrates have to be made for the proposed method, since the ordinary photo mask used for exposure is too large and heavy to be mounted on the fixture. These sacrificial masks can be made using the mask aligner. Standard i-line photoresists can be used for transferring the pattern on the ordinary photo mask to the sacrificial mask. After exposure using the mask aligner, bake, and develop, photoresist remains at the positions corresponding to the transparent part on the ordinary photo mask. Electron-beam evaporation or RF sputtering can be used for depositing Cr, which is a good opaque metal used on masks. After the lift-off process in acetone under ultrasonic agitation, the photoresist will be dissolved, and the Cr deposited on the

photoresist will be lifted off. And Cr adhered on the substrate will remain as the mask, so that we can obtain the same mask patterns as those on the original photo mask.

If the grating with the orientation of 0 degree to the x-axis (Figure 3-12) was fabricated first, the first sacrificial mask should mask all No. 1 pixels, so that the other pixels can be over-exposed and the photoresist will remain after the development. After that electron-beam evaporation will be used for depositing the Al film.

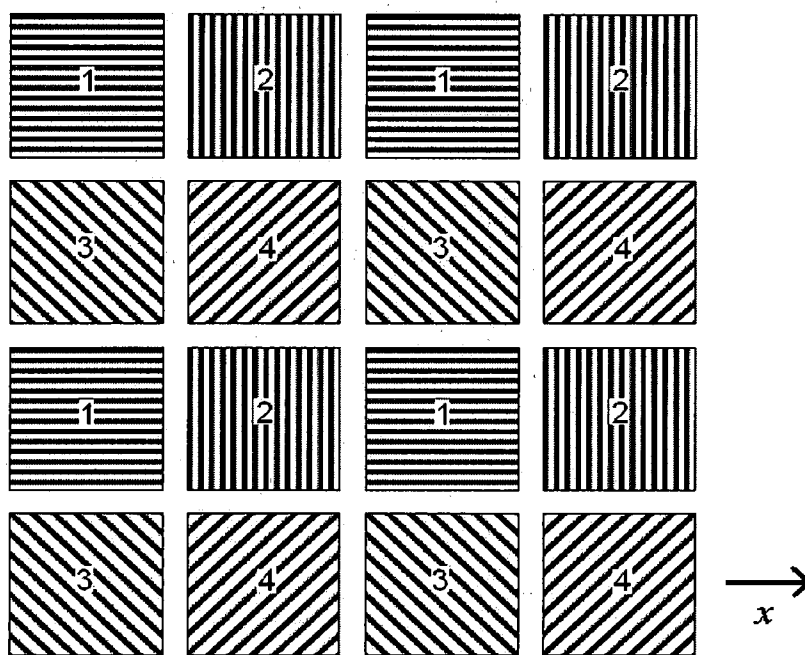


Figure 3-12. Pixels with pixel numbers

3.2.3 Electron-beam Evaporation Deposition

Just like thermal evaporation, in electron-beam evaporation, the source (deposition material) will be evaporated from the crucible, adhere to the substrate, and form a deposition layer. This is different from thermal evaporation, where the crucible is heated from below. Electron-beam evaporation heats the source from above using an electron beam to hit its top surface. Electron-beam evaporation will introduce less contamination, because the hottest part is the surface that is evaporating instead of the crucible in thermal evaporation.

As is shown in Figure 3-13 [18], a hot filament is used to create free electrons. After acceleration in the electric field built between the filament and the acceleration electrode, the electrons reach the source by bending under the magnetic field. A turbo-molecular pump and a dry mechanical pump are used to pump the chamber down to $\sim 10^{-7}$ Torr base pressure, which guarantees the purity of the film deposited. The process pressure of $\sim 10^{-5}$ Torr gives a mean free path longer than the dimension of the vacuum chamber, which makes the evaporated material hardly experience collisions on the way to the substrate. So the evaporated source goes through an almost straight path, the structure on the substrate will hardly have any sidewall coatings as happens in sputtering deposition. The nonconformity of the film makes it favorable for lift-off process.

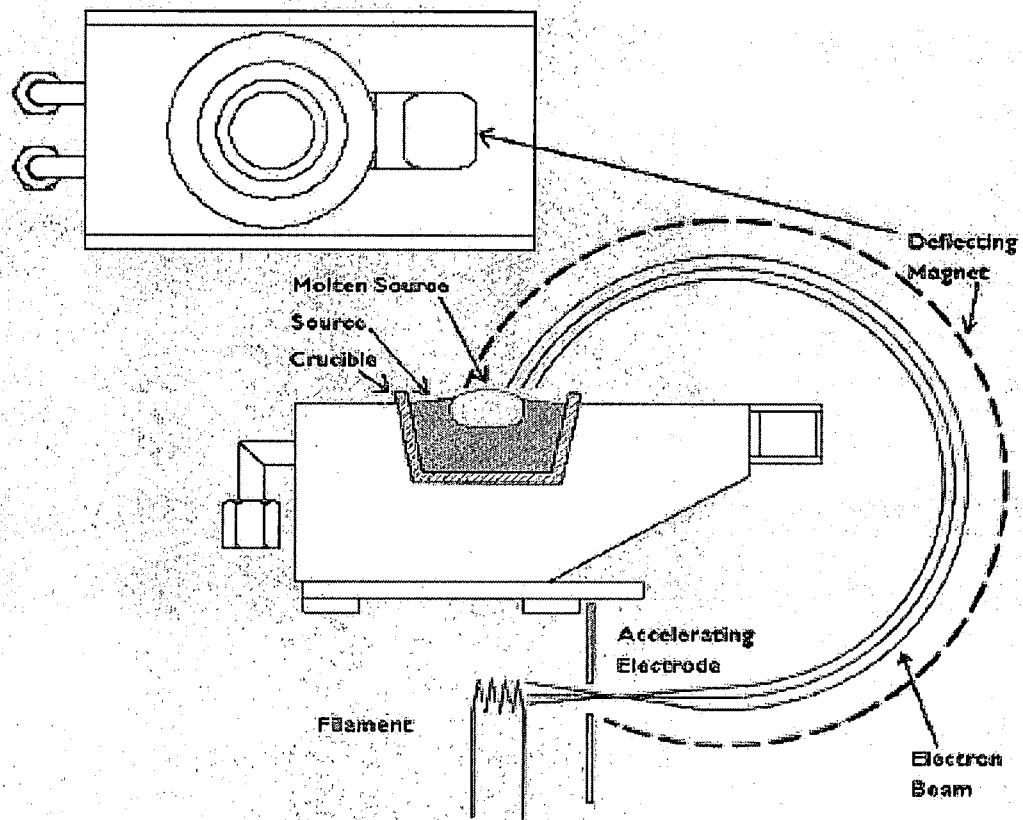


Figure 3-13. Principle of electron-beam evaporation deposition [18]

The deposition rate can be controlled by the number and velocity of electrons that bombard the surface of the source. The number of free electrons can be controlled by the current through the filament; and the velocity of free electrons can be controlled by the high voltage between the filament and the accelerating electrode. The more and the faster the electrons are, the higher the temperature of the source is, and the faster the deposition

rate is. But for most materials, fast deposition rate can increase the process pressure, which in turn increases the chance of side wall coating. So the deposition rate has to be controlled to a low value to avoid side wall coating and make the lift-off process easier.

3.2.4 Lift-off Process

In the lift-off process, acetone is used to dissolve the photoresist, so that the aluminum film deposited on the photoresist can be washed away from the sample. To enhance the lift-off process, the beaker with acetone is placed in an ultrasound water bath. After lift-off process, the aluminum grating will only exist on No. 1 pixel areas, since the aluminum deposited on the photoresist for the rest of the pixel areas is lifted off.

The above processes, spin coating UVN30, DUVLIL, over exposure with mask, development, electron-beam evaporation deposition, and lift-off, are for fabricating metal grating on the pixels with the same grating orientation, such as all No. 1 pixels. And then, the processes have to be repeated 3 times to fabricate metal grating with other orientations on the rest pixels. The only difference for each repeat is rotating the sample to achieve different grating transmission axes and using a different mask to mask different pixels. Figure 3-14 is a summary of the above processes.

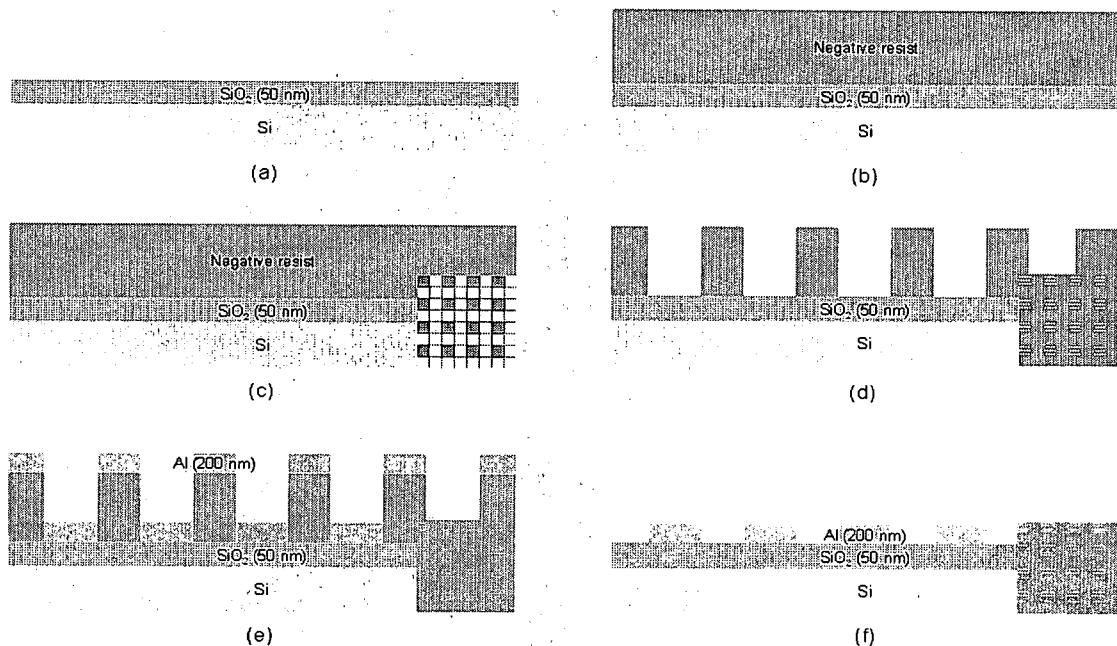


Figure 3-14. Diagrams of aluminum grating fabrication for pixels with the same orientation. (a) Diagram of cross sectional view of the silicon wafer after fabricating thin silicon dioxide layer, which is about 50 nm, on the silicon substrate using thermal oxidation; (b) Diagram of cross sectional view of the sample after spin coating UVN 30, which is negative photoresist for DUV; (c) After DUVLIL, using the mask shown as the inset to over expose the pixels for grating orientation other than the desired orientation; (d) Diagram of cross sectional view of the sample with top view diagram as an inset after development; (e) Diagram of cross sectional view of the sample with top view diagram as an inset after deposition of ~200 nm aluminum film using electron-beam evaporation. (f) Diagram of cross sectional view of the sample with top view as an inset after lift-off.

3.3 A Comparison of DUVPL and DUVLIL

In general, DUVLIL is a more flexible technique for grating parameter selections comparing to DUVPL. But DUVPL has a less complex fabrication process than DUVLIL.

For DUVPL, as discussed in Chapter III-1, the grating pattern is fixed, once the mask is designed and made. The grating parameters, such as grating period, cannot be changed. Moreover, with the limitation of the depth of focus, the thickness of photoresist is less than 400 nm, which in turn limits the grating thickness of the micropolarizer and hence limits the performance of the micropolarizer, especially the extinction ratio. Moreover, the size of a micropolarizer array is limited by the maximum field size. But the fabrication process is reliable and manufacturable. All the pixels with gratings of different orientations are fabricated in a single step exposure.

For DUVLIL, the grating parameters have more flexibility. The grating period can be changed by adjusting the angle between the sample surface and the incident beam. The grating duty cycle can also be changed by choosing different exposure doses. The grating height can be larger than 200 nm, since the interference pattern is not affected by diffraction through a mask. And much larger micropolarizer arrays can be fabricated by expanding the incident beam. However, the exposure process has to be achieved in four steps in order to fabricate gratings with different orientations, and sacrificial masks have

to be fabricated and aligned to the wafer for each step to over expose the pixels designed for other grating orientations. Furthermore, the quality of the process will degrade after each step because of the introduction of contaminants.

CHAPTER IV

MICROPOLARIZER CHARACTERIZATION

4.1 Introduction to a Tunable Infrared Laser Source

Nonlinear optics, different from linear optics and more complicated than linear optics, gives us many interesting phenomena that have many applications. The tunable IR laser source is one of these applications based on nonlinear optics.

In linear optics, nonlinear susceptibility or higher order susceptibility can be ignored. The dielectric polarization is proportional to electric field with linear susceptibility and permittivity of free space as the coefficient as shown in Equation (4.1).

$$\vec{P} = \epsilon_0 \vec{\chi} : \vec{E} \quad (4.1)$$

where \vec{P} is the polarization, \vec{E} is the electric field, ϵ_0 is the permittivity of free space, and $\vec{\chi}$ is linear susceptibility. Generally, \vec{P} and \vec{E} are vectors, and correspondingly $\vec{\chi}$ is a second-order tensor. In linear optics, the frequencies of input light beams cannot be changed. For example, there are two beams with frequencies of ω_1 and ω_2 participating

in a linear interaction. The frequencies of output beams can only be ω_1 and ω_2 , since only the linear term exists in the expression of polarization.

The most important difference between nonlinear optics interaction and linear optics interaction is whether new frequencies are generated during the interaction. In nonlinear optics, higher order susceptibility can not be ignored because of high electric field and large nonlinearity; and new frequencies are from the nonlinear terms of the expression of polarization. If the higher order response function is fast and instantaneous, which is valid for most situations, the polarization expression becomes

$$P(t) = \epsilon_0 \chi^{(1)} E(t) + \epsilon_0 \chi^{(2)} E^2(t) + \epsilon_0 \chi^{(3)} E^3(t) + \dots \quad (4.2)$$

The second order polarization for a specific orientation can be expressed as [22]

$$P^{(2)} = \epsilon_0 d_{eff} A_1(\pm\omega_1) A_2(\pm\omega_2) e^{i(\pm\omega_1 \pm \omega_2)t} + c.c. \quad (4.3)$$

where A_1 is the amplitude of the electric field with frequency of ω_1 , A_2 is the amplitude of the electric field with frequency of ω_2 , d_{eff} is the effective nonlinearity for the specified direction, and \pm indicates different frequency mixing processes.

Our tunable laser source is basically based on the second order polarization term. For two harmonic electric fields with frequencies of ω_1 and ω_2 , E^2 term will give new frequencies of $2\omega_1$ and $2\omega_2$ [second harmonic generation (SHG)], $\omega_1 + \omega_2$ [sum frequency generation (SFG)], and $\omega_1 - \omega_2$ [difference frequency generation (DFG)]. The

efficiency of nonlinear interaction is related to phase matching condition, the derivation of which is as follows [22].

From Maxwell's equations, we have

$$\nabla^2 \bar{E} = \mu \epsilon_0 \frac{\partial^2 \bar{E}}{\partial t^2} + \mu \frac{\partial^2 \bar{P}}{\partial t^2} \quad (4.4)$$

As shown in Equation (4.2), polarization term can be expanded into different orders.

$$\bar{P} = \bar{P}^{(1)} + \bar{P}^{(2)} + \bar{P}^{(3)} + \dots \quad (4.5)$$

If we only consider the first nonlinear polarization term, Equation (4.4) becomes

$$\nabla^2 \bar{E} = \mu \epsilon_0 \frac{\partial^2 \bar{E}}{\partial t^2} + \mu \epsilon_0 \chi^{(1)} \frac{\partial^2 \bar{E}}{\partial t^2} + \mu \frac{\partial^2 \bar{P}^{(2)}}{\partial t^2} \quad (4.6)$$

For each plane wave with frequency of ω_l ,

$$\mu \epsilon_0 [1 + \chi^{(1)}(\omega_l)] = \mu_0 \epsilon_0 n^2 = n^2 / c^2 \quad (4.7)$$

And then the wave equation for each frequency becomes

$$\nabla^2 \bar{E} - \frac{n^2}{c^2} \frac{\partial^2 \bar{E}}{\partial t^2} = \mu \frac{\partial^2 \bar{P}^{(2)}}{\partial t^2} \quad (4.8)$$

Plug Equation (4.7) into Equation (4.8), and consider DFG process of $\omega_1 \rightarrow \omega_2 + \omega_3$,

where ω_1 is the pump beam, ω_2 is the idler beam, and ω_3 signal beam. The wave equation for the signal beam is

$$\frac{d^2}{dz^2} \left[\frac{1}{2} A_3 e^{i(k_3 z - \omega_3 t)} \right] - \frac{n_3^2}{c^2} \frac{\partial^2}{\partial t^2} \left[\frac{1}{2} A_3 e^{i(k_3 z - \omega_3 t)} \right] = \mu \epsilon_0 d \frac{d^2}{dt^2} A_1 A_2^* e^{(k_1 - k_2)z - \omega_3 t} \quad (4.9)$$

Equation (4.10) can be simplified as

$$ik_3 \frac{dA_3}{dz} e^{ik_3 z} = -\omega_3^2 \mu \epsilon_0 d A_1 A_2^* e^{i(k_1 - k_2)z} \quad (4.10)$$

The equality of the phase terms on the two sides of Equation (4.11) gives phase matching condition, which is described by

$$\Delta k = k_1 - k_2 - k_3 = 0 \quad (4.11)$$

If we consider all the three wave equations, and solve the coupled equations in the undepleted pump regime (in this case both of the inputs are undepleted), we have the intensity of the signal beam

$$I_3 = \frac{\omega_3^2}{2\mu_0 n_3 c^3} d^2 |A_1|^2 |A_2|^2 L^2 \text{sinc}^2 \left(\frac{\Delta k L}{2} \right) \quad (4.12)$$

Equation (4.13) indicates how the phase matching condition affects the efficiency of the nonlinear interaction process (DFG process for this example).

There are several ways to achieve phase a matching condition [22]. For a birefringent crystal, pump beam, idler beam and signal beam with different polarizations may achieve phase matching condition, which is called birefringent phasematching. The second way is to align the input beams at an angle in order to minimize Δk , which is called noncollinear phasematching. The third way is quasi-phase matching (QPM), which uses the K vector of a periodic structure to compensate Δk . With the period of the crystal with periodic structure controllable, QPM increases the flexibility of phase matching. The tunable laser source is achieved by optical parametric generation (OPG) using QPM. OPG is like optical parametric amplification (OPA), which amplifies a signal

input in the presence of a higher-frequency wave, at the same time generates idler beam, and can be considered as DFG [23]. The difference between OPG and OPA is that there is no signal input for OPG. One pump wave input generates both signal wave and idler wave. And the initial signal (or idler) wave is from a zero-point quantum noise photon. Through amplification in the media with high gain, signal wave and idler wave are generated [22].

4.2 Experimental layout and description

Our IR laser source generated by an optical parametric generator (OPG) using a periodic poled lithium niobate (PPLN) crystal with wavelength tunable from 1.3 μm to 4.8 μm [24, 25]. The PPLN has eleven channels with different poling periods and the wavelength tunability is realized through switching channels. The experimental setup is illustrated in Figure 4-1.

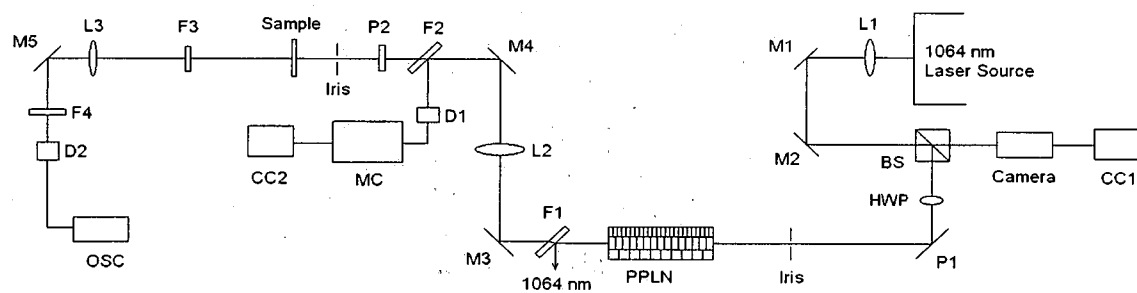


Figure 4-1. Experimental setup for optical characterization of micropolarizer. L1 to L3: lenses; M1 to M5: mirrors; BS: beam splitter; HWP: half-wave plate; P1: reflection polarizer; P2: transmission polarizer; F1 and F2: dichromatic filter; PPLN: periodically poled lithium niobate; D1 and D2: detectors; F3: filter for expanding the dynamic range of detector; F4: bandpass filter; MC: monochromator; CC1 and CC2: computer control using LabView; OSC: oscilloscope.

Lens L1 focuses the pump beam from a 1064 nm Nd:YAG nanosecond laser (Spectra-Physics Quanta-Ray) into one PPLN channel with the focal point at the center of that channel. A translation stage allows simple access to the different PPLN channels by positioning the crystal with respect to the pump beam. A camera is used to monitor the laser pointing. A half-wave plate (HWP) and reflection polarizer (P1) are used to adjust the power incident into the PPLN crystal. A signal beam and an idler beam are generated from the pump beam through the OPG process and the particular signal-idler pair is determined by the quasi-phase matching (QPM) period within the PPLN crystal. A lens

(L2) with a focal length of 20 cm, which is 40 cm away from the center of the PPLN crystal, focuses the beam that emerges from the PPLN onto the micropolarizer sample to be tested, which is also 40 cm from L2. The testing bar is used to characterize the micropolarizer. The filter F2 directs part of the signal beam to detector D1. With monochrometer (MC) and computer control (CC2), the wavelength of the signal beam is monitored. From the wavelength of the signal and the pump, the wavelength of the idler can be calculated based on energy conservation. The signal wavelength is between 1.3 μm and 1.7 μm , and the idler wavelength is between 2.9 μm to 4.8 μm . The idler beam is used to test our micropolarizer in the MWIR and the signal beam is used for the NIR test. Due to the QPM process, the output from the PPLN is linearly polarized and the extinction is better than the best IR polarizer we have. In the experiment, the transmission axis of the polymer polarizer P2 (InfraSpecs P03), which covers far-IR and mid-IR, is aligned in parallel with the polarization direction of the laser source to achieve polarization purity at least the same as the laser source. A lens (L3) focuses the beam to a size small enough to avoid overfilling the small sensor aperture of the detector. Filter (F3) is a calibrated attenuator used to expand the dynamic range of our extinction ratio measurement as described below. A band pass filter (F4) selects the desired single wavelength to reach the detector (D2). An EG&G HgCdTe detector is used for MWIR test and a Ge photodetector is used for the NIR. The detector output will be displayed on oscilloscope (OSC).

4.3 Measurement and Results

In order to characterize the micropolarizer, the sample was rotated to obtain p-polarization transmission T_p (the maximum transmission) and s-polarization transmission T_s (the minimum transmission). As the ratio of T_p and T_s is very large, a filter F3 was used to expand the dynamic range of our measurement. First, the signal T_p was measured with the filter F3 inserted to avoid saturating the detector. The signal is recorded to be V_p . Then the sample is rotated by 90 degrees to measure T_s . Since T_s is very small, the filter F3 has to be taken out to obtain a measurable signal, which is recorded to be V_s . The sample is rotated to obtain a large signal V_O just below the detector saturation level without the filter F3, so that enough signal can be obtained when the filter is inserted again in the last step. Finally, the filter F3 is inserted back into the setup, and the corresponding signal is recorded as V_F . From these measurements, the extinction ratio (ER) can be calculated by:

$$ER = \frac{V_p}{V_s} \frac{V_O}{V_F} \quad (4.13)$$

The experimental results along with the numerical simulation results are shown in Figure 4-2. In the 3 μm to 5 μm wavelength range, the measured extinction ratio is above 10^3 (30 dB). An extinction ratio as high as 3×10^4 was achieved for wavelengths near 5

μm . For shorter wavelengths around $1.5 \mu\text{m}$, the extinction ratio is still greater than 100 (20 dB). The TM transmission, T is around 70% in the $3 \mu\text{m}$ to $5 \mu\text{m}$ band, but for shorter wavelengths near $1.5 \mu\text{m}$, it drops to about 25%.

Although for longer wavelengths, the extinction ratio versus wavelength curve for measured results matches that for simulated results, the measured extinction ratios are about 1 order of magnitude lower than the simulation results for shorter wavelength range. For T_p versus wavelength, the measured results match the simulation results very well at the longer wavelengths, but are significantly smaller than predicted performance at shorter wavelengths. We attribute this discrepancy to the surface roughness of the metal grating and the deviation of refractive index from handbook values. Our extinction ratio measurement is limited by the low values of T_s . The scattering caused by the surface roughness of the grating will increase the T_s measurement and cause a lower extinction ratio measurement. At shorter wavelengths the period of the grating becomes comparable with the incident wavelength, making the micropolarizer more sensitive to surface roughness, non-ideal grating profile and other fabrication defects, which gives the discrepancy between the measurement and simulation results. Moreover, the actual refractive index of the deposited aluminum may be different from the values assumed in the model, which were obtained from standard handbook. A small difference in refractive index, especially the imaginary part, can cause appreciable discrepancy between the theoretical and actual performance of the micropolarizer.

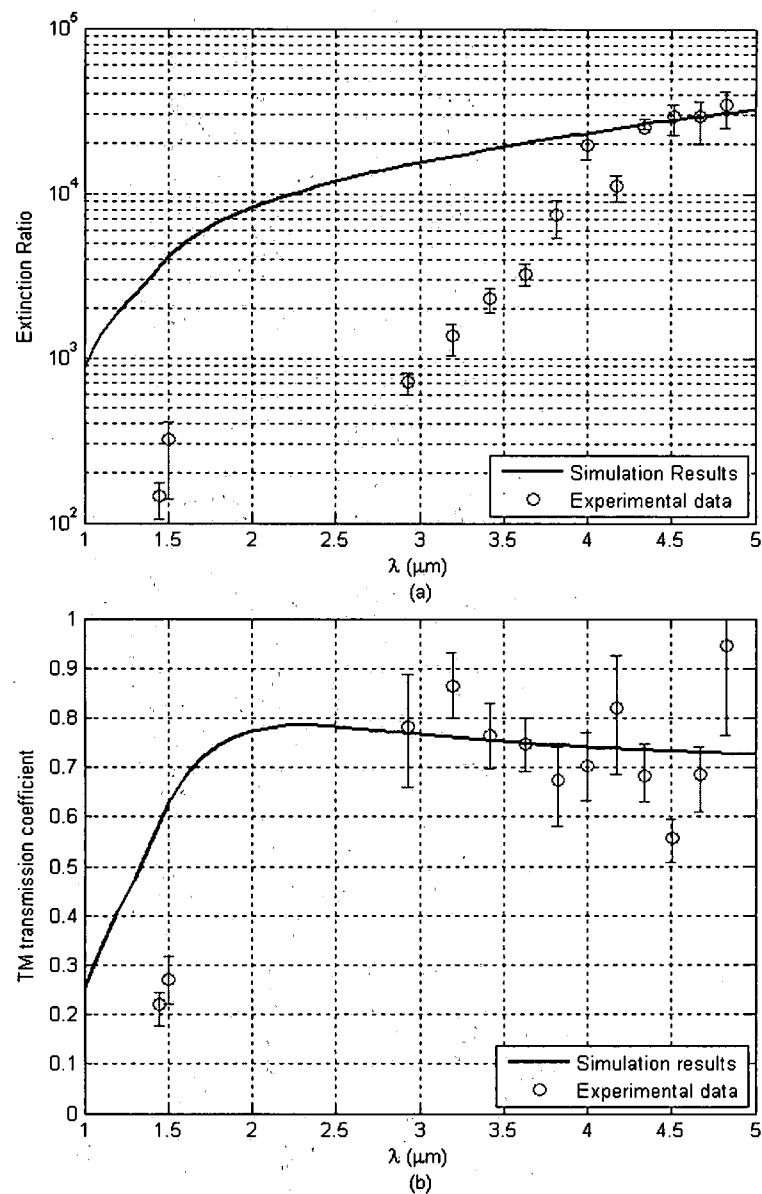


Figure 4-2. Experiment results of micropolarizer sample characterization along with simulation results. (a) Extinction ratio versus incident wavelength curve; (b) TM transmission coefficient versus incident wavelength curve.

CHAPTER V

CONCLUSIONS AND FUTURE WORK

Micropolarizer arrays have the capability to expand the electro-magnetic observables of IR imaging systems by including polarimetric information, such as the second and the third Stokes vector components. In this thesis, it has been shown that micropolarizer arrays can be obtained by grouping four wiregrid micropolarizers with different transmission axis orientations in a super pixel, which is similar to the way how color filtering is done in visible imaging. Each micropolarizer within a micropolarizer array is made of high spatial frequency metal grating with period smaller than the wavelength of incident light in the media. The subwavelength grating period enables these metal wiregrids to function as linear polarizers rather than diffraction gratings. The imaging performance of a micropolarizer array is determined by the figure of merit of micropolarizers, i.e. TM transmission and extinction ratio, which is in turn decided by the grating period, grating height, grating duty cycle and dielectric environment of the grating.

In order to investigate the optimal structure of the micropolarizer, RCWA modeling was performed to numerically simulate the performance of micropolarizers with different structure parameters. Under the fabrication limitations, the optimized design of micropolarizer structure has an aluminum grating with a grating period of 400 nm, a grating duty cycle of 0.7, and a grating height of 200 nm, and a thin silica layer with a thickness of 50 nm sandwiched between the silicon substrate and grating layer. This thin silica layer was specially designed for improving extinction ratio and TM transmission over a broad working wavelength range.

The fabrication technique applied for fabricating the micropolarizer array in this thesis, DUVPL, was introduced and discussed comparing with DUVLIL. With a relatively easier fabrication process, DUVPL lacks of the flexibility in terms of adjusting the structure of the micropolarizer array. The grating height is limited by the depth of focus, which is only 400 nm for enough resolution. The grating period is fixed once the mask is fixed. The array size is limited by the field size, which is good for 1M-pixel array. On the other hand, in DUVLIL with a multi-step fabrication process, the grating period can be easily changed from about 150 nm to several microns. The grating height can be larger because of the collimated coherent source provides an extremely long depth of focus. The array size is limited by the beam size and can be made up to 12.4M-pixels. But the contamination has to be well controlled in each step to minimize the degradation of fabrication quality.

A sample made by DUVPL technique was characterized with a tunable IR laser source generated by an optical parametric generator (OPG) using a periodic poled lithium niobate (PPLN) crystal with wavelength tunable from 1.3 μm to 4.8 μm . The measured results agree with the simulated results quite well in long wavelength range between 3 to 5 μm . The discrepancy at shorter wavelength range was attributed to the surface roughness, non-ideal grating profile and other fabrication defects of the metal grating and the deviation of refractive index from handbook values. At last, transmission coefficients for p-polarization greater than 70% are obtained with extinction ratios greater than 10^4 in the MWIR region. The extinction ratios are still greater than 10^2 for NIR region above 1.5 μm . The extinction ratio of our micropolarizer in MWIR region is about 2 orders of magnitude larger than the previous results.

For future work, the micropolarizer array will be fabricated using DUVLIL. The advantages and disadvantages of DUVPL and DUVLIL will be clearer through the comparison of the micropolarizer array samples fabricated with the two techniques. And then the fabricated micropolarizer array will be integrated with an InSb focal plane array and evaluated for its polarimetric imaging capabilities.

BIBLIOGRAPHY

1. Q. Zhan, "Polarization of Light" (class notes), EOP 665, Fall Semester, 2007.
2. T. J. Rogne, F. G. Smith, and J. E. Rice, "Passive target detection using polarized component of infrared signatures", in *Polarimetry: Radar, Infrared, Visible, Ultraviolet, and X-Ray*, R. A. Chipman and J. W. Morris, eds., Proc. SPIE **1317**, 242-251 (1990).
3. C. S. L. Chun, D. L. Fleming, and E. J. Torok, "Polarization-sensitive thermal imaging", in *Automatic Object Recognition IV*, F. A. Sadjadi, ed., Proc. SPIE **2234**, 275-286 (1994).
4. G. P. Nordin, J. T. Meier, P. C. Deguzman, and M. W. Jones, "Micropolarizer array for infrared imaging polarimetry", J. Opt. Soc. Am. A **16**, 1168-1174 (1999).
5. G. R. Bird, and M. Parrish, Jr., "The wire grid as a near-infrared polarizer", J. Opt. Soc. Am. **50**, 886-891 (1960).
6. I. Yamada, K. Kintaka, J. Nishii, S. Akioka, Y. Yamagishi, and M. Saito, "Mid-infrared wire-grid polarizer with silicides", Opt. Lett. **33**, 258-260 (2008).

7. J. J. Wang, L. Chen, X. Liu, P. Sciortino, F. Liu, F. Walters, and Xuegong Deng, "30-nm-wide aluminum nanowire grid for ultrahigh contrast and transmittance polarizers made by UV-nanoimprint lithography", *Appl. Phys. Lett.* **89**, 141105 (2006).
8. J. W. Goodman, *Introduction to Fourier Optics* (Roberts & Company, Englewood, Colorado, 2005) 3rd edition.
9. C. W. Haggans and L. Li, "Effective-medium theory of zeroth-order lamellar gratings in conical mountings", *J. Opt. Soc. Am. A* **10**, 2217-2225 (1993).
10. I. Richter, P.-C. Sun, F. Xu, and Y. Fainman, "Design considerations of form birefringent microstructures", *Appl. Opt.* **34**, 2421-2429 (1995).
11. D. L. Brundrett, E. N. Glytsis, and T. K. Gaylord, "Homogeneous layer models for high-spatial-frequency dielectric surface-relief gratings: conical diffraction and antireflection designs", *Appl. Opt.* **33**, 2695-2706 (1994).
12. P. Lalanne and J.-P. Hugonin, "High-order effective-medium theory of subwavelength gratings in classical mounting: application to volume holograms", *J. Opt. Soc. Am. A* **15**, 1843-1851 (1998).
13. M. G. Moharam, E. B. Grann, D. A. Pommet, and T. K. Gaylord, "Formulation for stable and efficient implementation of the rigorous coupled-wave analysis of binary gratings", *J. Opt. Am. A* **12**, 1068-1076 (1995).
14. M. G. Moharam, D. A. Pommet, E. B. Grann, and T. K. Gaylord, *J. Opt. Am. A* **12**, 1077-1086 (1995).

15. K. Knop, "Rigorous diffraction theory for transmission phase gratings with deep rectangular grooves", J. Opt. Soc. Am. **68**, 1206 (1978).
16. A. Taflove and S. C. Hagness, *Computational Electrodynamics: The Finite-Difference Time-Domain Method* (Artech House, Boston, 2005) 3rd edition.
17. E. D. Palik, *Handbook of Optical Constants of Solid* (Academic Press, San Diego, 1998).
18. A. M. Sarangan, "Nano-Fabrication Lab" (class notes), EOP 695, Spring Semester, 2008.
19. A. M. Sarangan, A. Mahfoud, Z. Wu, Q. Zhan, D. P. Forrai, D. W. Endres, J. W. Devitt, R. T. Mack, and J. S. Harris, "Wiregrid micro-polarizers for mid-infrared applications", SPIE Defense and Security Symposium **6959**, 695915 (2008).
20. Shipley, "UVN 30 Negative DUV Photoresist" (specification sheet), Shipley product literature, 1999.
21. Newport, "The Newport Resource 2006/2007" (Product Catalog), Vibration Control, 2006.
22. P. E. Powers, "Nonlinear Optics" (class notes), EOP 624, Spring Semester, 2008.
23. Wikipedia, "Nonlinear optics", <http://en.wikipedia.org/wiki/Nonlinear_optics>.

R002594042

24. J. J. Zayhowski, "Periodically poled lithium niobate optical parametric amplifiers pumped by high-power passively Q-switched microchip lasers", Opt. Lett. **22**, 169-171 (1997).
25. P. E. Powers, K. W. Aniolek, T. J. Kulp, B. R. Richman, and S. E. Bisson, "Periodically poled lithium niobate optical parametric amplifier seeded with the narrow-band filtered output of an optical parametric generator", Opt. Lett. **23**, 1886-1888 (1998).